AD-A188 093 PLASMA DEPOSITION OF SILICON CARBIDE THIN FILMS(U) 1/1
WESTINGHOUSE RESEARCH AND DEVELOPMENT CENTER PITTSBURGH
PA W D PARTLOW ET AL. 20 AUG 87 87-9C7-OPSIC-R1
UNCLASSIFIED AFOSR-TR-87-1693 F49620-84-C-0063 F/G 20/12 NL

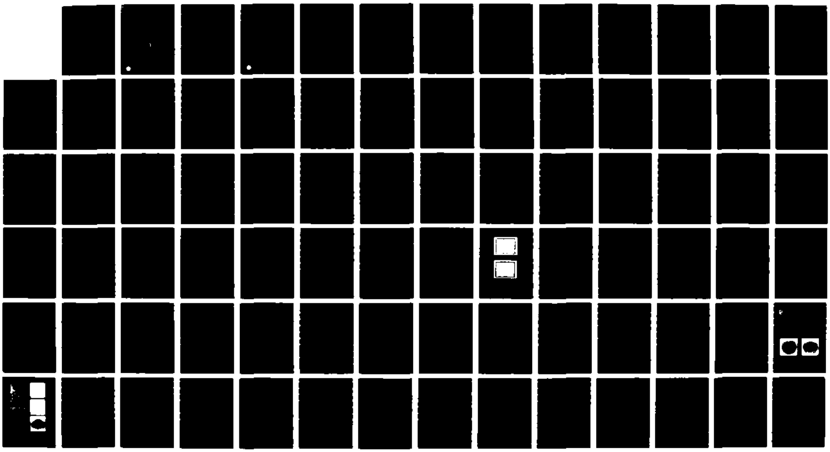

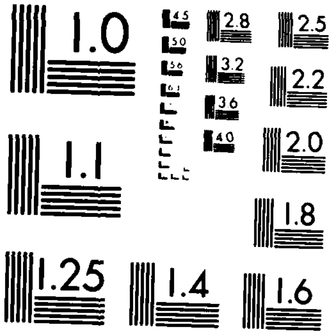

MICROCOPY RESOLUTION TEST CHART
NATIONAL BUREAU OF STANDARDS-1963-A

②

PLASMA DEPOSITION OF SILICON CARBIDE THIN FILMS

AFOSR-TR- 87-16

W. D. Partlow, W. J. Choyke, John T. Yates, Jr.,
L. E. Kline, M. J. Bozack, L. Muelhoff,
P. A. Taylor, A. Mascarenhas, J.V.R. Heberlein

Final Report
Report Period Covered
July 1, 1984 to July 31, 1987

Contract No. F49620-84-C-0063

August 20, 1987

Air Force Office of Scientific Research
Bolling Air Force Base
Washington, DC 20332

Captain Kevin J. Malloy
Program Manager

Westinghouse R&D Center
General Order Number WGD-11481-CE

DISTRIBUTION STATEMENT A
Approved for public release;
Distribution Unlimited

Westinghouse R&D Center
1310 Beulah Road
Pittsburgh, Pennsylvania 15

SECURITY CLASSIFICATION OF THIS PAGE

REPORT DOCUMENTATION PAGE

1a. REPORT SECURITY CLASSIFICATION
Unclassified

1b. RESTRICTIVE MARKINGS

2a. SECURITY CLASSIFICATION AUTHORITY

2b. DECLASSIFICATION / DOWNGRADING SCHEDULE

3. DISTRIBUTION / AVAILABILITY OF REPORT
Unlimited

4. PERFORMING ORGANIZATION REPORT NUMBER(S)
87-9C7-OPSIC-R1

5. MONITORING ORGANIZATION REPORT NUMBER(S)
AFOSR-TR- 87-16

6a. NAME OF PERFORMING ORGANIZATION
Westinghouse R&D Center

6b. OFFICE SYMBOL (If applicable)

7a. NAME OF MONITORING ORGANIZATION
Air Force Office of Scientific Research

6c. ADDRESS (City, State, and ZIP Code)
1310 Beulah Road
Pittsburgh, PA 15235

7b. ADDRESS (City, State, and ZIP Code)
Bolling AFB
Washington, DC 20332

8a. NAME OF FUNDING / SPONSORING ORGANIZATION Air Force Office of Scientific Research

8b. OFFICE SYMBOL (If applicable)

9. PROCUREMENT INSTRUMENT IDENTIFICATION NUMBER
F49620-84-C-0063

8c. ADDRESS (City, State, and ZIP Code)
Bolling AFB
Washington, DC 20332

10. SOURCE OF FUNDING NUMBERS

PROGRAM ELEMENT NO.	PROJECT NO.	TASK NO.	WORK UNIT ACCESSION NO.
61102F	2306	B2	

11. TITLE (Include Security Classification)
Plasma Deposition of Silicon Carbide Thin Films

12. PERSONAL AUTHOR(S)
W. D. Partlow, W. J. Choyke, John T. Yates, Jr., L. E. Kline (see title page)

13a. TYPE OF REPORT
Final

13b. TIME COVERED
FROM 7/1/84 TO 7/31/87

14. DATE OF REPORT (Year, Month, Day)
1987, August 20

15. PAGE COUNT

16. SUPPLEMENTARY NOTATION

17. COSATI CODES

FIELD	GROUP	SUB-GROUP

18. SUBJECT TERMS (Continue on reverse if necessary and identify by block number)

19. ABSTRACT (Continue on reverse if necessary and identify by block number)

This report summarizes the work performed on a three year program to obtain an understanding of deposition processes of thin films from plasmas. Deposition plasmas of methane and of methane-hydrogen and methane-silane mixtures were characterized via electrical, optical, and mass spectroscopic measurements. Surface chemical studies of the fundamental surface reactions were performed, and a model was constructed which takes into account both gas phase and the surface processes leading to deposition. The properties of the deposited films were related to the plasma conditions associated with their deposition. Advances in process modeling and surface chemical techniques were achieved on this program, in addition to the knowledge that was gained about the specific plasma deposition processes that were studied.

20. DISTRIBUTION / AVAILABILITY OF ABSTRACT
☐ UNCLASSIFIED/UNLIMITED ☐ SAME AS RPT ☐ DTIC USERS

21. ABSTRACT SECURITY CLASSIFICATION
Unclassified

22a. NAME OF RESPONSIBLE INDIVIDUAL
Mallory

22b. TELEPHONE (Include Area Code)
(202) 767-4932

22c. OFFICE SYMBOL
NE

DD FORM 1473, 84 MAR 83 APR edition may be used until exhausted.
All other editions are obsolete

SECURITY CLASSIFICATION OF THIS PAGE

PLASMA DEPOSITION OF SILICON CARBIDE THIN FILMS

W. D. Partlow, W. J. Choyke, John T. Yates, Jr.,
L. E. Kline, M. J. Bozack, L. Muelhoff,
P. A. Taylor, A. Mascarenhas, J.V.R. Heberlein

Final Report
Report Period Covered
July 1, 1984 to July 31, 1987

Contract No. F49620-84-C-0063

August 20, 1987

Air Force Office of Scientific Research
Bolling Air Force Base
Washington, DC 20332

Captain Kevin J. Malloy
Program Manager

Westinghouse R&D Center
General Order Number WGD-11481-CE

Westinghouse R&D Center
1310 Beulah Road
Pittsburgh, Pennsylvania 15235

CONTENTS

PLASMA DEPOSITION OF SILICON CARBIDE THIN FILMS

ABSTRACT

This report summarizes the work performed on a three year program to obtain an understanding of deposition processes of thin films from plasmas. Deposition plasmas of methane and of methane-hydrogen and methane-silane mixtures were characterized via electrical, optical, and mass spectroscopic measurements. Surface chemical studies of the fundamental surface reactions were performed, and a model was constructed which takes into account both gas phase and the surface processes leading to deposition. The properties of the deposited films were related to the plasma conditions associated with their deposition, and new interpretations of the characterization data were obtained based on the dual phase nature of the films. Advances in process modeling and surface chemical techniques were achieved on this program, in addition to the knowledge that was gained about the specific plasma deposition processes that were studied.

1. INTRODUCTION

The objective of this program was to understand the fundamental processes for deposition of thin films from plasmas in order to control the properties of the films through process control. It consisted of three thrusts:

a. Experimental characterization and modeling of deposition plasmas,
b. Characterization of deposited films and relation of the film properties to the plasma conditions,
c. Investigation of surface chemistry of elementary deposition processes.

Plasma deposition of thin films, and characterization of the plasmas were carried out at the Westinghouse R&D Center. Dr. L. E. Kline of the R&D Center collaborated in these investigations by developing a plasma model on a corporate-funded program and applying the model to deposition plasmas. Characterization of the films was mostly carried out at the R&D Center, with some assistance from the Physics Optics Laboratory at the University of Pittsburgh. The surface chemistry investigations were performed in the Surface Science Center in the Department of Chemistry at the University of Pittsburgh. Central program management and coordination of the different tasks was provided by the Westinghouse R&D Center.

2. SUMMARY AND CONCLUSIONS

We designed and carried out plasma characterization and deposition experiments that provided data which was sufficient to define the conditions of the plasmas, compositions and ion species and energies, that have important impact on the properties of the films. The experiments were performed on a research reactor that had been upgraded to facilitate the extensive characterization. It permitted deposition of films under different conditions in the same plasma, and on different substrates under the same plasma conditions. The plasma modeling gave us insight into the physical and chemical processes leading to thin film deposition.

Most of the experiments and modeling were done on the deposition of hydrogenated carbon films from methane, because of the excellent dissociation and chemical reaction data available for this widely used combustion gas. Less extensive studies were carried out on methane-hydrogen mixtures, and on mixtures of methane and silane used for the deposition of amorphous silicon carbide. We arrived at a consistent model of methane plasmas which permitted us to establish the most likely chemical reaction paths and surface processes involved in deposition, and to estimate the sticking coefficients of key species. This work provided understanding of important process issues such as how to achieve uniformity of deposition, and how to avoid gas phase nucleation. The modeling of gas mixtures pointed out important process issues uniquely associated with how mixtures affect process control.

Deposited films were characterized by several optical techniques: spectrophotometry over the UV, visible, and near infrared regions, Fourier transform spectroscopy in the far infrared, and Raman spectroscopy. Transmission electron microscopic measurements were also made. We determined from these measurements that dual phase carbon films containing microcrystals in an amorphous matrix were obtained under conditions of high ion bombardment. These hard, stable materials contrast with amorphous films produced under low ion bombardment which react with the atmosphere to acquire carbonyl and hydroxyl features in their infrared spectrum. We found that the infrared feature near 2930cm^{-1} appears in both types of films, is probably associated with the amorphous component of the films.

The surface studies attacked the most basic aspects of deposition processes: fundamental chemical reactions of adsorbed hydrocarbon species with silicon surfaces. At the outset of the program, very little work had been done in this area, so the research methods had to be developed. The subsequent study determined that the C=C bond reacts with dangling bonds on the surface, and that these reactions can be controlled by techniques in which the surface is bombarded with ions or electrons, or passivated with atomic hydrogen. The surface studies also provided guidance to the modeling effort in establishing likely surface deposition processes and estimating the sticking coefficients of the important species.

The impact of the program as a whole has been multifold, including the following items:

a. advancing the techniques for process control and modeling, specifically for deposition processes, but also for plasma processes in general,
b. development of techniques for studying surface reactions,
c. development of a working plasma model that can be used for many other applications,
d. advancing the knowledge of the structure of amorphous and microcrystalline carbon films, and how their properties are controlled by the plasma conditions,
e. advancing the knowledge of the chemistry of organic species on surfaces,
f. advancing the capabilities of the university laboratories and of the students involved in the program,
g. cementing an effective industrial-university relationship.

Numerous publications have resulted from this program, including journal articles, conference proceedings, invited talks, and contributed conference papers. These are listed in references 1 through 13. We are currently preparing two more manuscripts for publication based on this work.

The following sections of this report discuss the technical output of this program in detail. It is presented in a different perspective than the technical papers that report the work. Emphasis is placed on explaining to the reader the insights on how the measurements were made, what we were trying to find out, and how the experiments compare to the models from an overview perspective. This is done in an effort to convey the current status of understanding of this research. The reader is referred to the publications for more details and documentation of the different components of the program.

3. EXPERIMENTS AND MODELING OF PLASMAS

3.1. Introduction

The objectives of the characterization and modeling of the plasmas are explained with the aid of Fig. 3.1. By gaining an understanding of the physical and chemical processes in the plasma, we can relate the process characteristics to the actual processes (shown in the box of Fig.3.1) rather than to the process control variables (shown on the left) as is done in conventional parametric studies. This basic approach is particularly effective in advancing the technology in the future through the work of others, as well as ourselves, via the deeper understanding obtained. In the case of plasma processing, this approach is especially important because of the severe difficulty of transferring results from one plasma reactor to another, e.g. in process scale-up. Since the operating conditions of reactors vary widely, and common parameters are often not available, it is important to understand exactly which conditions need to be created in the reactor. In the following subsections we will describe the experimental apparatus and techniques, and then the plasma model. This will be followed by a discussion of the results that we obtained for methane, methane-hydrogen mixtures, and methane-silane mixtures.

3.2 Experimental Measurements: CH_4 Plasmas

The deposition apparatus was designed to provide the information that is crucial to defining the deposition conditions adequately to permit modeling of the electron dissociation and chemical kinetics of the process, namely:

a) gas pressure,
b) reactant gas flow rates, hence velocity, residence time,
c) product gas composition,

d) deposition rates,
e) RF plasma excitation voltage, current, power,
f) electrode bias voltages,
g) electric field variation between electrodes,
h) electrode temperature.

The system, designed around 4" Pyrex pipe vacuum components, is shown schematically in Fig. 3.2. Several interchangeable electrodes were provided. The upper electrode shown in Fig. 3.2 has a floating probe diagnostic consisting of a 1 cm^2 disc extending into the plasma. It is used to measure the floating probe potential that can be used to estimate the plasma potential. The lower (coaxial) electrode is designed for achieving high electrode bias which results in high energy ion bombardment of the sample during film growth. Electrode bias values depend on geometry, power, pressure, and gas composition, generally increasing when electron losses at the electrode are increased by increasing power, reducing pressure, or reducing the area of the electrode relative to grounded surfaces in the reactor. Fig. 3.3 shows an example of the dependence of the self bias potential of the RF-powered coaxial electrode on excitation power, along with the peak-to-peak applied voltage and the floating probe potential. The negative bias is nearly one half of the peak-to-peak excitation voltage, so the plasma characteristics approach those of a diode, having 100% effective asymmetry. The floating probe potential is 10-20V below the plasma potential[14], so grounded surfaces in the plasma are at potentials of only several tens of volts from the plasma. We took advantage of this asymmetry to produce thin film samples under different conditions within the same plasma, and also on different types of substrates. A set of deposition electrodes built to achieve this is shown in Fig. 3.4. Both silicon and fused silica substrates were mounted on the coaxial lower electrode and the grounded upper electrode , providing samples with high and low energy ion bombardment respectively from the same plasma. The fused silica substrates are used for UV, visible, and near infrared spectrophotometric characterization of the films, and the silicon wafer substrates are suitable for infrared and Raman characterization.

Measurements of product gas compositions are crucial for understanding and controlling the process chemistry, and for testing the chemical models. Compositions were estimated from mass spectrometric measurements of the exhaust gases taken with the differentially pumped sampling system that is shown in Fig. 3.2 about 0.6 m downstream from the plasma. Most of the reactive species have recombined by the time the gases reach the sampling unit, so comparisons of the mass spectra to those of stable pure gases are relevant. We used such comparisons to estimate the partial pressures of CH_4, C_2H_4, C_2H_6, C_3H_8, H_2,and C_4H_{10}. Fig. 3.5 shows an example of raw data from the mass sampler for CH_4 at a constant flow rate for several values of excitation power. With no plasma power applied, the CH_4 cracking pattern is seen in the vicinity of mass 16 along with false lines of CO^+(28) and $CO_2{}^+$(44) that are associated with the materials in the quadrupole mass spectrometer head. H, H_2, and C_2H_X fragments produced by the ionizer in the mass spectrometer are also seen. The lower traces show the spectra for two levels of plasma excitation power, with the production of increasing amounts of higher hydrocarbons at higher powers. We were able to resolve the group near mass 28 into its C_2H_4 and C_2H_6 components based on calibrations with pure gases. The hydrocarbons with three or more carbon atoms were not resolvable, so we chose a mass line to represent each carbon multiple group, such as C_3H_X, and calibrated against an available stable member of the group such as C_3H_8. Plots, thus obtained, of the species densities in the downstream gases versus excitation power and flow rate are shown in Figs. 3.6 and 3.7. In Fig. 3.6 the decrease of CH_4 reactant and increase of dissociation products is seen to increase with excitation power. Fig. 3.7 shows that for higher flow rates, with less specific energy (joules/molecule), lower densities of product species are seen. Substrates were weighed before and after deposition to determine deposition fluxes. This is mainly a measure of the carbon deposition flux since the carbon atom is 12 times as heavy as the hydrogen atom. Deposition fluxes correlated with electrode bias, as shown in Fig. 3.8. Higher deposition fluxes are seen on the higher biased electrode, and fluxes increase at higher powers as do biases. A fairly weak dependence of deposition flux on flow rate is seen, as illustrated by Fig. 3.9. We found the deposition fluxes to be uniform over the 5 cm silicon wafers to within about 5%, indicating that variation of deposition rate along the flow lines of the plasma was less than 10%.

The mass spectroscopic and deposition rate data were combined to determine the total mass transport of carbon in the reactor, as shown in Fig. 3.10. At high flow rates, carbon input was found to be equal to carbon output within experimental error. At low flow rates, all of the carbon entering the reactor could not be accounted for in the deposited films and the product gases. We suspect that this is due to nucleation of particles directly from the gas phase, which is known to occur at high specific energy excitation.[15] Thus, the mass transport data gives us a technique for determining regions of operation where this (usually undesirable) volumetric nucleation occurs. It also provides input to the model about the net fluxes of the species to the surface, information which is especially needed since there is very little data for estimating such processes a priori.

Electrical measurements, especially of the excitation power, are necessary for characterizing the plasma. These are not trivial measurements at the frequencies used to operate the plasmas, typically 1MHz or higher. Plasma excitation power supplies normally are equipped with directional power meters that operate in the 50 ohm transmission line between the RF generator and the impedance matching network (see Fig. 3.2). Unfortunately, power dissipated in the matching network is measured by these meters, along with the power delivered to the plasma. The former can be a significant fraction of the total power. We therefore made direct measurements of the voltage and current waveforms of the plasma and integrated their product with a Tektronix Model 7854 sampling oscilloscope which performs the calculation on line. An oscillogram of the voltage, current, and product waveforms thus obtained is shown in Fig. 3.11. These waveforms are also needed for modeling the time and space dependences of the electron dissociation processes.

modeling the time and space dependences of the electron dissociation processes.

We made optical spectroscopic measurements of the visible atomic hydrogen emission lines (Balmer series) and of the emission bands of the CH radical. Absolute radiometric measurements served as an independent check of the electron kinetics model, particularly, the branching of the CH_4 dissociation into H and CH respectively. We also measured the spatial variation of the plasma luminosity from one electrode to the other with a traversing radiometer which imaged a slice of the plasma on a slit-masked detector. An example is shown in Fig. 3.12. The sharp feature shown at the powered electrode, position: 30 mm, is associated with the surface of the electrode. The broader feature extending to the grounded electrode at 10 mm results from the volumetric dissociation of CH_4, and can be compared to the spatial predictions of the model.

3.3 Modeling of CH_4 Plasmas

Plasma modeling was done as a collaborative effort by L. E. Kline of the Westinghouse R&D Center and was supported by Westinghouse corporate funding, but we will describe it briefly here since it was so closely coupled to the experiments, and provided guidance and feedback to the experimental plasma measurements.

The model couples a Monte Carlo simulation (MCS) of the electron kinetics of the RF discharge to a plug flow model of the gas phase chemical kinetics in a plasma reactor. The MCS follows the trajectories of 1000 to 2000 electrons as they are accelerated by the local electric field and scattered, losing energy, in elastic and inelastic collisions. The electric field variation in time and space was simulated according to the diagram shown in Fig. 3.13, where it varies sinusiodally at all positions. This is based on the spectroscopic measurements made by ourselves and others.[16] A plug flow rate equation model is used to predict the densities of CH_4 and the intermediate and product species as a function of position measured in the flow direction. The species densities are averaged in the direction perpendicular to the gas flow.

The net rates of diffusion to the electrodes including the effect of reflection and sticking of species at the electrode surfaces are estimated by using a formulation developed by Chantry.[17] The resulting set of coupled ordinary differential equations for species densities versus position is solved using the Gear stiff equation solver.[18] Electron impact, neutral-neutral, ion-molecule, and surface reactions were included in the rate equations, and are listed in one of our publications.[9] Homogeneous reaction rate coefficients for neutral species were obtained mainly from a recent critical compilation by Tsang and Hampton et. al. of the NBS.[19] Ion neutral rate coefficients are from a review by Albritton et. al.[20] Since there is no quantitative data for surface reactions, probable reactions were assumed and sticking coefficients were varied to fit the experimental mass transfer data. Guidance for the assumptions was obtained from the data and the experience of our surface science coworkers at the University of Pittsburgh. By requiring the predicted deposition to be uniform along the flow lines over a wide range of flow values as was observed experimentally, and adjusting sticking coefficients to provide the measured deposition rates, sufficient boundary conditions were available to fully define the surface deposition kinetics.

The model thus obtained predicts the downstream species densities versus gas residence time that are shown for CH_4 operated at 15 watts in Fig. 3.14 along with the experimental values for the stable product species. These dependences are depicted realistically. The dominant kinetic pathways for this case that lead to film growth and downstream species are represented in Fig. 3.15 out of a total of 44 reactions used in the model). It is seen that CH_3 is the dominant deposition precursor in this example, having a sticking coefficient of 0.03. The very reactive species CH_2 and CH do not appear in Fig. 3.15 even though their production rates are significant. The predicted densities of these species are small because CH_2 is quickly converted to CH in reactions with H atoms, and CH produces C_2H_5 by reacting even more rapidly with CH_4. Even with sticking coefficients of unity, no significant deposition would result from these species.

3.5 Results: CH_4-H_2 Mixtures

A series of samples were deposited in mixtures of CH_4 and H_2 to determine the effects of the addition of H_2 on both the plasma and the deposited films. These experiments are of interest for several reasons. Firstly, for comparison to pure methane plasmas. The effect of adding H_2 on the CH_4-H_2 ratios in the plasma, as shown in Fig. 3.16, is similar to lowering the flow rate in CH_4 plasmas, shown in Fig. 3.7. Also, recent work in the deposition of carbon in the diamond phase at high temperatures[21,22] in large excesses of hydrogen, and some reports indicating that there may be some benefits at low temperatures[23,24] as well, led us to investigate these mixtures.

Using the same electrode configuration that we used for CH_4 deposition experiments, we deposited thin films in mixtures ranging from 1% to 100% CH_4 in H_2. Deposition rates at constant power of 15W are shown in Fig. 3.17 as determined by weighing the substrates before and after deposition. For high CH_4 fractions, higher deposition rates are seen on the lower, more highly biased electrode, but for low CH_4 fractions the situation reverses and in fact the deposition rate becomes negative. The substrate has been etched on the highly bombarded, lower electrode and not on the weakly bombarded, upper electrode, where the deposition rate has remained positive and is independent of CH_4 concentration. At these low CH_4 concentrations, deposition on the upper electrode is probably due to chemical vapor transport of silicon from the lower electrode.

Another observation that we made on the mixtures has a major influence on the properties of the films. The self bias voltage increases as H_2 is added to the CH_4, then decreases again at very low CH_4 concentrations, as shown in Fig. 3.18. Again, a corresponding similarity is seen in the bias voltage of CH_4 plasmas at low flow rates, where increased bias voltages are also measured.

3.6 Results: CH_4-SiH_4 Mixtures

Data were taken on plasmas consisting of mixtures of 10% SiH_4 in CH_4 for the deposition of amorphous silicon carbide, and the plasma modeling calculations were performed on the electron dissociation and chemical kinetics. Deposition rate data showed a behavior similar to methane, in that higher deposition rates were obtained on the biased electrode than on the grounded one, as illustrated in Fig. 3.19. The flow dependence was markedly different. Deposition rate increases were seen at low flow rates, compared to the CH_4 case where deposition rates were nearly independent of flow rate, as shown in Fig. 3.9. Gas species calibrations were performed the same way as for the CH_4 plasmas. Reactions and rate coefficients for SiH_4 were added to the model, and a comparison of the predictions of the model to the experimental measurements is shown in Figs. 3.20 for hydrocarbon species. C_2H_X species have about the same densities as were found in CH_4 plasmas, but C_3H_X species are much lower, indicating that it may be depleted in forming $SiCH_x$ species that we observe. Silicon containing species, shown in Fig. 3.21, show considerably more depletion at long residence times than the hydrocarbons. The SiH_4 fragments do not have a significant back reaction analogous to CH_4^+ and CH_3 in methane plasmas, which react to replenish CH_4. Three sets of theoretical curves are shown in this figure. They were obtained using three values of the reaction coefficient for the $H + SiH_4$ reaction, a significant factor in depleting SiH_4. The larger value provides better predictions of SiH_4 densities, while the smaller value predicts Si_2H_x densities better. We have some doubts about the accuracy of our extrapolations of the rate coefficients, measured at high pressures, to the low pressure conditions of our experiments. The model does however, provide realistic qualitative predictions of the trends and of the high SiH_4 depletion at long gas residence times.

4. FILM CHARACTERIZATION

We characterized the optical properties of deposited films with UV-visible spectrophotometric measurements, Fourier transform infrared absorption measurements, and transmission electron microscopy. We investigated the dependence of film properties on plasma power, gas composition, and pressure. Most measurements were made on the hydrogenated carbon films produced in methane plasmas, but also films produced in methane-hydrogen gas mixtures were investigated.

4.1 UV-Visible Spectrophotometry

The optical band gap and the refractive index were determined from spectrophotometric measurements of the optical density of films deposited on clear fused silica substrates. Refractive index, n, and film thickness, t, were determined from the interference maxima and minima of the spectra measured in the near infrared, and the absorption coefficient thus determined was fitted to the Tauc relation[25] to determine the optical gap. The raw data for a carbon film deposited from a methane plasma is shown in Fig. 4.1 plotted with two ordinate scales. The film is clear in the visible and near infrared, with an absorption edge in the near UV. The refractive index, n, of the film is determined from the maximum value of the interference undulations, and the optical thickness, nt, is determined from the locations of the peaks[26] assuming n to be constant over the range fitted. This is a very good approximation. Using the thickness thus obtained, the absorption constant, a, was fitted to the Tauc relation as shown in Fig. 4.2. A good straight line fit is observed for high values of SQRT(a*E), with a significant departure at low values due to tailing of the band states. The extrapolation of the straight region of the curve is used to estimate the optical gap, which is seen to be about 2 eV for this sample.

The optical gaps thus determined were compared for films deposited from the plasmas. Figure 4.3 shows the Tauc plots for two carbon films deposited from the same plasma, but from the two different electrodes, which have different ion bombardment conditions as we discussed in Section 3. The sample from the powered electrode with a bias potential of 400V, and comparable ion energies, has an optical gap of about 0.8eV, whereas the sample from the grounded electrode, subjected to only low energy ions, has a gap of about 2eV. This dependence of optical gap on electrode bias has been reported by earlier workers.[27] Low gap values in the 1eV range are associated with so-called "hard carbon", with desirable hardness and chemical inertness that makes them useful for protective and tribological coatings. The higher gap materials are softer and, as we shall see later, react with the atmosphere to form hydrates and carbonyls. Figure 4.4 shows similar Tauc plots for films deposited at a lower power for the same gas pressure, where the bias voltage is lower. We see higher optical gaps for films deposited on both electrodes, reflecting the lower plasma potential as well as a lower self bias voltage for the powered electrode. A similar effect is seen in Fig. 4.5, where lower bias voltage and plasma potential have been achieved by increasing the gas pressure to 1 torr. Figure 4.6 shows the Tauc plots for films deposited in mixtures of methane and hydrogen at constant power and pressure. Decrease in optical gap is seen for lower concentrations of methane in hydrogen. This correlates with the increasing plasma voltages with reduced methane concentration. Consistently, all changes of plasma parameters influence the film properties via their influence on the plasma voltage and bias potential.

Refractive index values of the films also reflect the ion bombardment associated with the deposition conditions. Carbon films produced on the highly biased electrode, e.g. 350V, typically have refractive index values of 1.9-2, while films produced at lower biases and on the grounded electrode have refractive index values as low as 1.55.

4.2 Infrared Spectra

The infrared spectra of two carbon films, deposited from the same plasma on silicon wafers located on the grounded and powered electrodes respectively, are shown in Fig. 4.7. The different periodicities of the interference maxima and minima reflect the fact that the film deposited at the powered electrode has a higher deposition rate, as we pointed out in Section 3. Superimposed on these sinusiodal variations, distinct absorption peaks are seen at slightly below 3000 cm^{-1} which are due to the C-H vibrational stretch modes, and several peaks below 1500 cm^{-1} due to CH_2 and C-C stretching modes, C-H bending modes, and strong peaks in the silicon wafer substrate that were not completely subtracted out of the data. The data shown in Fig. 4.7 were taken several hours after deposition, on samples that were stored in a dry nitrogen-flushed atmosphere until measurement. Exposure to air introduces major changes in the infrared spectrum of the lightly bombarded films, but no change in the heavily bombarded ones from the biased electrode. The spectra of the same samples shown in Fig. 4.7 were re-measured after about 5 weeks exposure to air, and are shown in Fig. 4.8. The largest bands acquired by the lightly bombarded sample are at 1700cm^{-1} and 3400cm^{-1}, and are attributed to carbonyl (C=O) and water respectively. In both samples the C-H stretch mode frequencies peak at about 2930 cm-1, characteristic of carbon which is mostly sp3 hybridized. This assignment is based on the invariance of bond group frequencies in different molecules,[28] and deconvolution studies of the C-H band in a-C:H films.[29] Thus, the ion bombardment does not have a major effect on the bond hybridization of the films, but it has a major effect on the physical properties of the films, such as refractive index, chemical stability, and hardness. To find out more about the way ion bombardment affects the films, we investigated electron optics techniques, as discussed in the next section.

4.3 Electron Optics

Transmission electron diffraction micrographs and diffraction patterns of the heavily and lightly bombarded films are shown in Fig. 4.9. The lightly bombarded samples show a fine-grained microstructure and diffuse diffraction patterns characteristic of amorphous materials, while the heavily bombarded sample shows a dual phase structure of microcrystals of about 50 in size imbedded in an amorphous matrix, similar to the structure reported by Spencer et. al.[30], with sharper diffraction rings over a diffuse background. A closer examination of the TEM of the heavily bombarded films is shown in Fig. 4.10. Dark field photographs, which select only one orientation, reveal only a fraction of the microcrystals, indication that they have a large distribution of orientations, as implied by the ring diffraction patterns. The positions of the sharp diffraction rings correspond to those of diamond, and the easily recognizable ring from the graphite "sliding plane" is absent.

4.4 Characterisation Conclusions

The properties of the films deposited from methane and methane-hydrogen plasmas are influenced by most of the available experimental parameters: power, pressure, electrode geometry, and composition. The effects of changing these parameters can be understood by considering their influence on the plasma sheath potential, which controls the ion bombardment of the growing film surfaces.

Combining our infrared and electron optics results, it is clear that a major difference between the "hard carbon" that we deposit under conditions of high ion bombardment, and the soft, chemically unstable material produced in the absence of this bombardment, is the dual phase structure of the former, consisting of microcrystals of diamond in an amorphous matrix. These differences are not obvious from the infrared analysis of the C-H mode, which indicates similar bonding hybridization for the two types of materials. It is reasonable to conclude that the infrared absorption technique mainly sees the amorphous matrix, and not the microcrystals, since the hydrogen content of the amorphous matrix would be expected to be much higher than hydrogen impurities in the crystalline diamond component. These results also lead us to suspect that the UV-visible optical properties are also characteristic of the amorphous matrix, rather than of the crystals. If the desirable properties hard carbon films are mainly due to the microcrystalline component, then there are avenues for improvements in these materials by altering the composition, structure, and quantity of the amorphous matrix which appears to be the cause of many of its undesirable properties.

5. SURFACE STUDIES

5.1 Introduction

The study of the elementary steps and the chemical species responsible for the surface chemical reactions at work in thin film CVD and PVD deposition processes is in its infancy. At the present time the CVD and PVD processes are controlled through knowledge gained by practical experience rather than by understanding of well-established surface chemical principles. This project has dealt with this issue by attempting to simplify the situation at the substrate surface so that individual elementary surface phenomena could be studied, one at a time. The production of silicon carbide thin films from the interaction of hydrocarbons with Si(100) is the particular chemical process selected for study here, but the principles may apply to other chemical systems as well, (i.e. Si_3N_4 films). We have developed research methods which work well in ultrahigh vacuum for the study of the interaction of hydrocarbon molecules with active sites on Si(100). It has been discovered that the C=C bond in olefinic molecules is a strongly active bond center for reaction with dangling bond sites on the Si(100) surface. We have learned how to control the C=C reactive chemistry at these dangling bond sites, either enhancing the reaction to produce SiC thin films or turning off the reaction. In addition, exploratory studies of the effect of electron bombardment on SiC thin film production have been made.

5.2 Development of Experimental Methods

5.2.1 Vacuum System Design

It has been necessary to learn how to work with single crystals of Si in ultrahigh vacuum in order to study carefully the surface chemistry which occurs. Figure 5.1 shows a schematic picture of the apparatus developed. A single crystal of Si is mounted on a manipulator which can be positioned at any angle within the chamber. The crystal temperature can be controlled from about 77 K to about 1500 K. An Auger spectrometer combined with the use of an ion gun for sputtering, and with controlled heating in vacuum, has been shown to produce clean Si(100) surfaces. Most experiments are performed at the position of the quadrupole mass spectrometer (QMS). Here, four types of investigations can be carried out:

1. Adsorption of gases from a molecular beam doser while monitoring the reflected gas from the crystal surface as a function of time (and coverage).
2. Thermal desorption of molecules from the surface upon heating the crystal in a temperature-programmed fashion.
3. H atom capping (Si-H bond formation) of active sites on the Si(100) surface using a hot filament to dissociate $H_2(g)$ and to deliver H atoms, line-of-sight, to the crystal surface.
4. Electron bombardment of the surface containing adsorbed species followed by temperature programmed desorption to investigate the chemical effect and cross section for surface species' damage.

5.2.2 Crystal Mounting

In order to carry out these experiments, we have devised a unique crystal mounting scheme, shown in Figure 5.2, which permits the surface chemistry of the crystal to be studied without interference from hot metal heating leads. The Si(100) crystal is slotted on three edges with a diamond saw. In the two opposite slots, Ta internal spring contacts are fabricated such that they contact the crystal with good ohmic and thermal contact by internal spring pressure. The third slot also contains a Ta spring which has a thermocouple junction welded inside, again making good thermal contact with the crystal. The assembly is mounted on a sapphire block electrical insulator which is inserted in a well in a Cu block which is cooled to 77 K. This rather elaborate procedure provides the following advantages:

1. Good ohmic and thermal contact.

2. Isolation of the Si surface from line-of-sight exposure to hot metal surfaces which could produce oxide film deposits. Elimination of possible activation of organic molecules being deposited from the molecular beam by hot metal surfaces.

5.2.3 Crystal Heating

Resistive heating of semiconductors is complicated by the temperature-dependent decrease in resistivity of semiconducting material. In the absence of current control at a critical temperature, a runaway situation can develop, leading to destruction of the crystal. For this reason, a feedback technique is needed, and a controller to do this is shown in Figure 5.3. This device can be preset for a desired limiting temperature, and is then used for annealing the crystal at its high temperature limit.

For crystal temperature programming, we sometimes use radiative heating from a lamp which is focused through a window onto the crystal. Heating up to about 900 K may be achieved using f/1.32 optics and a magnification of unity. Recently, a digital temperature controller has been developed in our laboratory which can also be used to ohmically heat the crystal, and we plan to publish this design soon, since precise temperature ramping of semiconductors is an uncommon and desirable laboratory capability.

5.2.4 Molecular Beam Methods

We employ a collimated molecular beam doser for two kinds of experiments:

1. Study of the reflected flux of reactant molecules as adsorption proceeds, yielding adsorption kinetics.
2. Precise and accurate dosing of the crystal with a known flux of adsorbate molecules, prior to other experiments.

A schematic diagram of the molecular beam dosing apparatus is shown in Figure 5.4. Here a micron orifice is used to limit the gas flow rate through the doser which is directed at the single crystal. A back pressure of one torr yields about 5 x 10^{13} molecules/cm^2sec at the crystal surface. The flux is known and reproducible to about 3%. The beam originating from the end of the doser is fairly well collimated by a microchannel plate collimator array and therefore delivers a rather uniform dose across the crystal.

As will be discussed later, we employ temperature programmed desorption to characterize the kinetics of desorption of adsorbates from the crystal surface. A multiplexed quadrupole mass spectrometer is employed for this, and may be set to rapidly sample multiple masses during the temperature programmed desorption process, and hence to rapidly determine the chemical identity of all volatile products of the surface reaction(s). An example of the desorption behavior of propylene, C_3H_6, as a function of increasing exposure to propylene is shown in Figure 5.5.

The use of temperature programmed desorption is combined in this apparatus with Auger spectroscopy studies of the surface in order to determine the behavior of carbon-containing species on the surface which do not desorb. In order to do this, we utilize the Auger spectrometer, making duplicate measurements at various locations on the crystal surface to improve the quality of the Auger data.

5.3 Chemical Reactivity of the C=C Bond on Si(100)

5.3.1 Introduction

There have been only a few studies of the interaction of organic molecules with silicon in which definite patterns of chemical reactivity have been characterized. At elevated temperatures such as those employed in CVD processes, it is likely that a wide range of chemical reaction steps occur together as the gas molecules crack down thermally to fragment gas phase, and surface species. The unraveling of these processes, in our view, begins with the study of the low activation energy surface chemical processes which occur at low temperatures, followed by a cautious and controlled advance into the high temperature regions. The determination of whether the C-C single bond, the C-H single bond, or the C=C double bond is the active site for low activation energy surface chemistry was one of our first experimental goals.

In order to understand the activity of the three selected classes of chemical bonds involving C in organic molecules, three kinds of experiments were performed:

1. A molecule containing the THREE types of C bonds was used as a test molecule for interaction with Si(100).
2. A similar molecule containing only TWO of the types of C bonds was compared in surface reactivity.
3. A third molecule, containing only ONE type of chemical C bond was compared in surface reactivity.

5.3.2 Experimental Results- Hydrocarbon Adsorption on Si(100)

Figure 5.6 shows the results of our adsorption kinetic and Auger measurements comparing the three classes of C chemical bonds as discussed briefly above. Here, the atomically clean Si crystal is rotated into a molecular beam of the test gas, and the reflectivity of the crystal for each molecule is determined as a function of gas exposure. The first experimental plot shows that when Si(100) at 120 K is rotated into a beam of propylene, C_3H_6, containing C=C, C-C, and C-H bonds, evidence for initial rapid gas uptake with a constant sticking coefficient (estimated to be about 1) is observed. This initial fast reaction region is immediately followed by a slower kinetic process producing an asymptotic region in the mass spectrometer signal-versus-time plot. Following adsorption, Auger spectroscopy indicates that C-containing species are present, and that the Si Auger signal is attenuated compared to the clean surface, as would be expected for an adsorption process.

The second panel (Fig.5.6) shows a test of propane, C_3H_8 containing only C-C bonds and C-H bonds. NO REACTION IS OBSERVED. The third panel tests methane, CH_4, containing only C-H bonds. NO REACTION IS OBSERVED.

Thus these experiments show that at low temperatures, it is only the C=C functional group which possesses the ability to react with surface valencies on Si(100). These results have recently been confirmed using the ethylene molecule, C_2H_4, and will be reported soon. In addition, we have recently found that the carbon-carbon triple bond, present for example in acetylene, C_2H_2, is also active at low temperatures for reaction with Si(100), and these results are being readied for publication.

Auxiliary studies of the influence on surface defect formation (by ion bombardment) on inducing surface reactivity at low temperatures with the unreactive molecules, propane and methane, have been negative. However, a significant variation in the reactivity pattern of propylene is observed upon sputter damage of the surface, as will be discussed later.

5.3.3 Thermal Chemistry for Propylene on Si(100).

The liberation of propylene from the Si(100) surface upon temperature programming of the crystal above 120 K is shown in Figure 5.5. ONLY A FRACTION OF THE PROPYLENE IS BONDED TO THE Si(100) SURFACE IN A FORM WHICH LIBERATES PROPYLENE UPON THERMAL DESORPTION. This is shown in Figure 5.7 in which Auger spectroscopy is used to monitor the C/Si ratio at the surface as a function of exposure to propylene. In this measurement, the C/Si Auger ratio before and after propylene desorption is determined for all exposures of the surface to propylene. IT CAN BE SEEN THAT THROUGHOUT THE FULL COVERAGE RANGE OF PROPYLENE, ABOUT 35% OF THE PROPYLENE DESORBS WHILE 65% REMAINS AS SURFACE C, WHICH ULTIMATELY DEGRADES TO SiC. These two channels for surface reactivity will be discussed later.

5.3.4 Effect of Surface Disordering on the Behavior of Si(100) in its interaction with Propylene

The bombardment of Si(100) with 2 kV Ar ions has been found to strongly influence the adsorption kinetics of the propylene reaction with the surface, suggesting that the presence of active sites on the surface is of importance. As shown in Figure 5.8, the desorption channel involving propylene is slowly attenuated as the extent of surface damage is increased. Here the propylene desorption state decreases in coverage monotonically as the surface damage by Ar ions increases. The reduction in the capability of the surface, following damage, to liberate C_3H_6 is shown in Figure 5.9. It is observed that little change in Si surface reactivity occurs for Ar ion fluences below 10^{12} ions/cm^2. However, with additional prebombardment, the propylene desorption yield falls steadily to an asymptotic value near zero, which is reached when about 10^{15} ions/cm^2 have collided with the surface. On the basis of these data, we have calculated the cross section per Ar ion for the damage process leading to the attenuation of the propylene desorption channel, obtaining a cross section, $\Phi = 2.7 \times 10^{-15}$ cm^2.

These results indicate that disordering of the Si surface can influence the course of a surface reaction rather profoundly, and that the effect is rather local, since the remaining quantity of propylene which desorbs is not perturbed significantly in its desorption kinetics as evidenced by the constancy on the peak temperature in Figure 5.8.

5.3.5 Effect of Preadsorbed Hydrogen on the Reaction of Propylene with Si(100)

Current evidence suggests that at low coverage, H adsorption on Si(100) at room temperature initially produces a monohydride surface species with a (2 x 1) LEED structure. At saturation coverage, a disordered phase has been observed, with roughly half of the H bonded in the monohydride phase and half in the dihydride phase.

We have studied the influence of hydrogen on Si surface chemistry by exploring the effect of atomic hydrogen preadsorption on the adsorption and thermal desorption of propylene from Si(100). The results indicate that preadsorption of H passivates the surface of Si and suppresses the reaction with propylene. Varying preexposures of atomic H were followed by addition of a constant dose of propylene. The resulting thermal desorption curves for propylene are shown in Figure 5.10. Here it is seen that preexposure to atomic H causes a reduction in the propylene yield, accompanied by a broadening of the desorption peak and a slight shift to higher temperature. Further studies of the kinetics of adsorption of propylene on the H-precovered surface, using the molecular beam method like that shown in Figure 5.6, indicate the effect is caused by a reduction in the adsorptive capacity for propylene.

5.3.6 Effect of Electron Bombardment on Propylene Adsorbed on Si(100)

The effect of electron irradiation on the thermal desorption behavior of propylene on Si(100) is shown in Figure 5.11. Here, it is seen that electron irradiation causes a decrease in the yield of propylene produced by thermal desorption, but no change in desorption kinetics occurs over the range of the effect. A plot of the yield of propylene versus the electron fluence (electron energy = 20 eV) is shown in Figure 5.12, and a monotonic decrease in the desorption of propylene is seen to occur. A cross section for this process was estimated using standard methods, and the cross section was found to be 4×10^{-18} cm^2 for the process. Auxiliary studies using Auger spectroscopy have show that propylene layers on Si(100) exhibit changes in Auger lineshape during electron bombardment, showing that the electron irradiation is not just desorbing propylene from the surface but is causing a significant bonding change for the C atoms present on the surface.

5.3.7 A Tentative Model of C=C Interaction with Si Sites on Si(100)

It is well known from recent scanning tunneling microscopy results that annealed Si(100) can contain approximately 20 % defect sites as judged by the examination of surface topography. Let us imagine that the defect sites are divided into two basic types:

Type A: Single Si-dangling bonds in the range of the C=C bond in the test molecule, C_3H_6.

Type AA: Double Si-dangling bonds in the same range.

C_3H_6 adsorption on a single dangling bond site (Type A) leads to surface structure A while adsorption on site AA leads to structure AA.

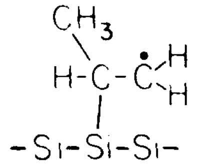

Structure A

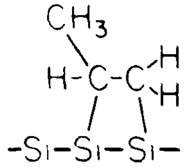

Structure AA

Upon adsorption at 130 K, either structure A or structure AA forms, depending on the type of site encountered. Structure A will exhibit a high activation energy for desorption of C_3H_6 as the Si-C bond breaks to reform the C=C bond, which releases the propylene from the surface in the high temperature desorption state shown in Figure 5.5, where analysis of the desorption feature has yielded an activation energy of 1.2 eV. In contrast, structure AA is so strongly bound to the surface through two C-Si bonds that cracking of the molecule occurs upon heating to produce surface fragments which eventually produce a SiC thin film.

Thus in this tentative model, C_3H_6 adsorption samples only dangling bond sites of the two types.

If this model is correct, then three predictions can be made and these can be compared to experimental results:

PREDICTION I: Ion bombardment will increase the number density of double dangling bond sites (AA) at the expense of single dangling bond sites. This should decrease the ability of the surface to desorb molecular propylene. PREDICTION IS VERIFIED.

PREDICTION II: Capping of dangling bond sites by atomic hydrogen will decrease the reactivity of the Si surface, causing both the propylene desorption channel and the SiC production channel to become less significant. PREDICTION IS VERIFIED.

PREDICTION III: Electron bombardment of a propylene layer will cause molecular fragmentation of the C_3 species leading to attenuation of the propylene desorption channel and to a change in C Auger lineshape. PREDICTION IS VERIFIED.

This simple picture which is consistent with our experimental findings at the present stage of our experiments needs to be verified by surface spectroscopic studies and such studies are planned for the future.

6. REFERENCES

1. W. D. Partlow and L. E. Kline, "Experiments and Modeling of Methane-Silane Plasmas", 1985 IEEE Conference on Plasma Science, Pittsburgh, PA, June, 1985.

2. L. E. Kline and W. D. Partlow, "Measured and Predicted a-C:H Deposition Rates in RF Discharges in CF4", 38th Annual Gaseous Electronics Conference, Monterey, CA, October, 1985.

3. M. J. Bozack, P. A. Taylor, W. J. Choyke, and J. T. Yates, Jr., "Chemical Reactivity of the C=C Double Bond on Silicon Surfaces", Surface Science 177, L933, (1986).

4. W. D. Partlow and L. E. Kline, "Homogeneous and Heterogeneous Chemistry of Methane Deposition Plasmas", Proceedings of the 1986 Spring Meeting of the Materials Research Society, Symposium C: Plasma Processing (Vol 68).

5. W. D. Partlow, "Plasma CVD: New Ways to Control Thin Film Deposition Processes", Invited Paper, SPIE 30th Annual Conference on Optical and Optoelectronic Applied Sciences and Engineering, San Diego, CA, August, 1986.

6. M. J. Bozack, W. J. Choyke, L. Muelhoff, and J. T. Yates, Jr., "Reaction Chemistry at the Si(100) Surface - Control Through Active Site Manipulation", J. Appl. Phys. 60, 3750, (1986).

7. J. T. Yates, Jr., M. J. Bozack, L. Muelhoff, and W. J. Choyke, "Control of Surface Reactivity of the Si(100) Surface", Invited Paper, 1986 MRS Meeting, to be published.

8. L. E. Kline, W. E. Bies, and W. D. Partlow, "Measured and Predicted Light Emission From RF Discharges in CH4", 39th Annual Gaseous Electronics Conference, Madison, WI, October, 1986.

9. Laurence E. Kline, William D. Partlow, and William E. Bies, "Electron and Chemical Kinetics in Low Pressure RF Discharge Deposition of Amorphous Carbon Films", Proceedings, Electrochemical Society Sixth Symposium on Plasma Processing, San Diego, CA, October, 1986.

10. M. J. Bozack, L. Muelhoff, J. N. Russell, Jr., W. J. Choyke, and J. T. Yates, Jr., "Methods in Semiconductor Surface Chemistry", J. Vac. Sci. and Tech. A5, 1, 1987.

11. W. D. Partlow and L. E. Kline, "Experiments and Modeling of Methane Plasmas", Fourth North Coast Symposium, Ohio Chapter of the AVS, Cleveland, OH, May, 1987.

12. W. D. Partlow and L. E. Kline, "Physics and Chemistry of Methane Deposition Plasmas", Invited Paper, Second Annual Diamond Technology Initiative Seminar, Durham, NC, July, 1987.

13. L. E. Kline and W. D. Partlow, "Electron and Chemical Kinetics in Low Pressure RF Discharge Deposition of Amorphous Silicon Carbide Thin Films", 8th International Symposium on Plasma Chemistry, Tokyo, September, 1987.

14. Brian Chapman, "Glow Discharge Processes", P.53, 69, John Wiley and Sons, New York, 1980.

15. K. G. Spears and R. M. Roth, Proceedings of the Materials Research Society 1985 Fall Symposium, "Plasma Synthesis and Etching of Electronic Materials", Vol. 38, p.111, November, 1985.

16. R. A. Gottscho and C. E. Gabe, IEEE Transactions on Plasma Science PS-14, 92, (1986).

17. P. J. Chantry, "A Simple Formula For Diffusion Calculations Involving Wall Reflections and Low Density", J. Appl. Phys. 62, 1141, (1987).

18. C. W. Gear, "Numerical Initial Value Problems in Ordinary Differential Equations", Prentiss Hall, Englewood Cliffs, 1971.

19. W. Tsang and R. F. Hampson, NBS Report NBSIR 84-2913, June, 1985.

20. D. L. Albritton, Atomic Data and Nuclear Tables 22, 1, (1978).

21. B. V. Spitsyn, L. L. Builov, and B. V. Derjaguin, "Vapor Growth of Diamond on Diamond and Other Surfaces", J. Cryst Growth 52, 219, (1981).

22. S. Matsumoto, Y. Sato, M. Kamo, and N. Setaka, "Vapor Deposition of Diamond Particles From Methane", Japan J. Appl. Phys., 21, L183, (1982).

23. Kazutaka Fujii, Nobuaki Shotaha, Masao Mikami, and Masatomo Yonezawa, "Properties of Carbon Films by DC Plasma Deposition", Appl. Phys. Lett. 47(4), 370, (1985).

24. Charles B. Zarowin, Natarajan Venkataramanan, and Richard R. Poole, "New Diamondlike Carbon Film Deposition Process Using Plasma Assisted Chemical Vapor Transport", Appl. Phys. Lett. 48(12), 759, (1986).

25. J. Tauc, R. Grigorovici, and A. Vancu, "Optical Properties and Electronic Structure of Amorphous Germanium", Phys. Stat. Sol.15, 627, (1966).

26. Fredrick Wooten, "Optical Properties of Solids", Academic Press, New York (1962).

27. A Bubenzer, B. Dischler, G. Brandt, and P. Koidl, "RF-Plasma Deposited Amorphous Hydrogenated Hard Carbon Thin Films: Preparation, Properties, and Applications", J. Appl. Phys. 54(8), 4590, (1983).

28. Gerhard Herzberg, "Molecular Spectra and Molecular Structure II, Infrared and Raman Spectra of Polyatomic Molecules", D. Van Nostrand and Co. Princeton, N. J.

29. B. Dischler, A. Bubenzer, and P. Koidl, "Bonding in Hydrogenated Hard Carbon Studied by Optical Spectroscopy", Solid State Comm. 48 No. 2, 105, (1983).

30. E. G. Spencer, P. H. Schmidt, D. C. Joy, and F. J. Sansalone, "Ion-Beam-Deposited Polycrystallind Diamondlike Films", Appl.Phys. Lett. 29 No. 2, 118, (1976).

7. ACKNOWLEDGEMENTS

The authors wish to express their appreciation to R. A. Madia for technical assistance in all of the plasma deposition experiments. Acknowledgements are also due to D. H. Lemmon for taking the Fourier transform infrared data, J. Greggi for the TEM data, and William E. Bies for assisting in the plasma modeling tasks.

FIGURE CAPTIONS

3.1 Relation between process control variables, process characteristics, and the fundamental physical and chemical processes that control the process.

3.2 Schematic of the deposition apparatus, showing some of the associated plasma diagnostics.

3.3 Relations between average negative bias of the powered electrode, floating probe potential, and peak-to-peak plasma excitation voltage as a function of power.

3.4 Experimental deposition electrodes, showing positions of substrates.

3.5 Example of raw mass spectrometric data, taken downstream of the plasma, as a function of power.

3.6 Dependence of species densities versus power.

3.7 Dependence of species densities versus flow rate.

3.8 Carbon deposition flux versus power at constant flow rate.

3.9 Carbon deposition flux versus flow rate at constant power.

3.10 Example of mass transport of carbon in the reactor at methane flow of 30sccm, power 15W.

3.11 Typical waveforms of the 2MHz plasma excitation. Upper photo: sinusiodal curve is voltage at 500V/cm, peaked curve is current at 100ma/cm. Lower photo: instantaneous power at 1W/cm.

3.12 Photocurrent of detector measuring relative radiance (radiant exitance) of the plasma as a function of position along the axis. Lower, powered electrode at 32mm, upper electrode at 12mm.

3.13 Assumed E/n values (electric field to gas density ratio) versus position at several times within the RF cycle.

3.14 Measured and predicted species densities versus time.

3.15 Dominant kinetic pathways and species in methane plasmas.

3.16 Species densities versus methane concentration in methane-hydrogen plasmas, 30sccm, 15W.

3.17 Deposition rate versus methane concentration in methane-hydrogen plasmas, 30sccm, 15W.

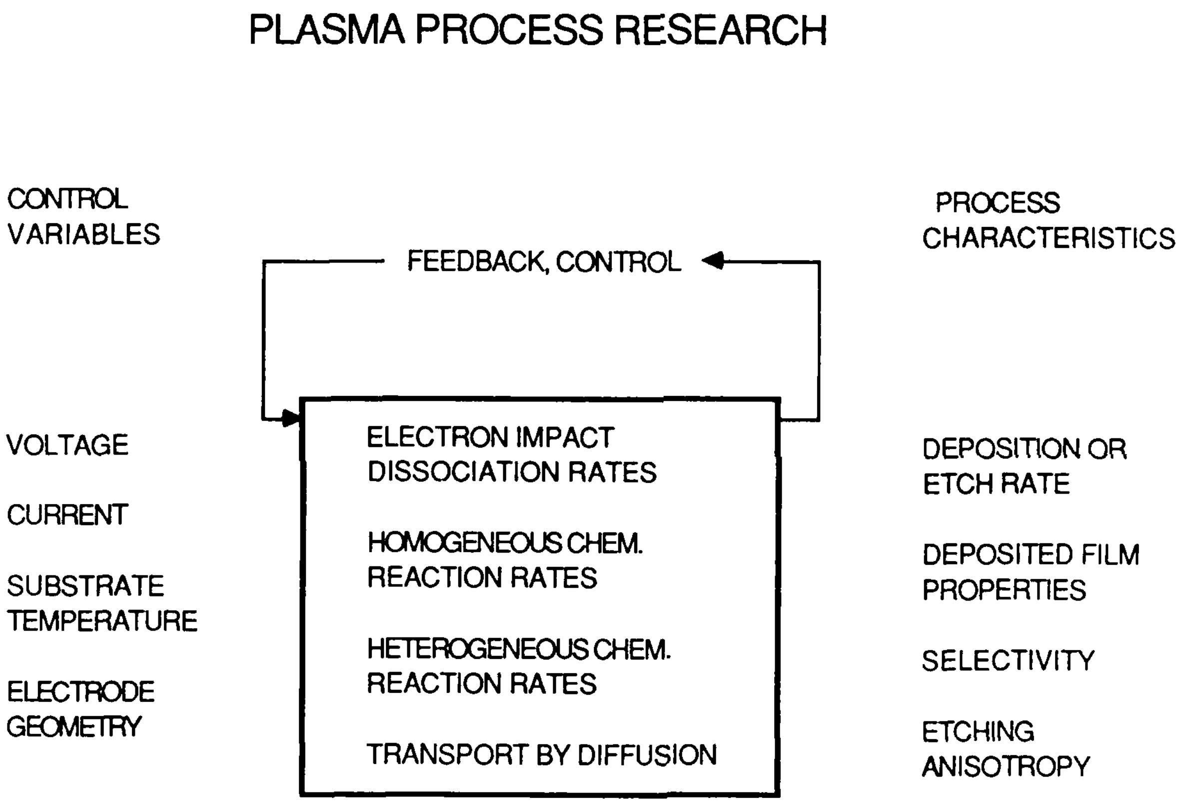

Figure 3.1 - Relation between process control variables, process characteristics, and the fundamental physical and chemical processes that control the process.

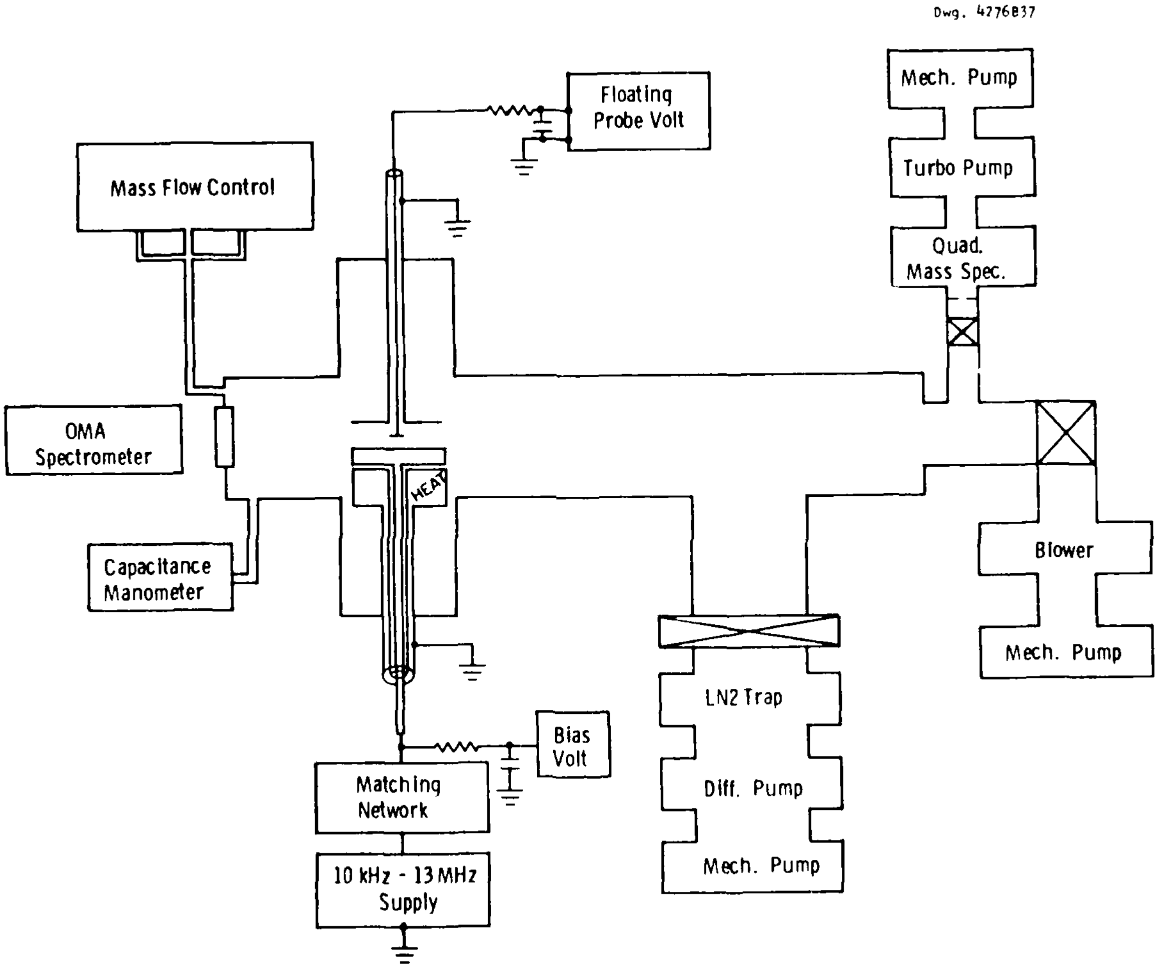

Figure 3.2 - Schematic of the deposition apparatus, showing some of the associated plasma diagnostics.

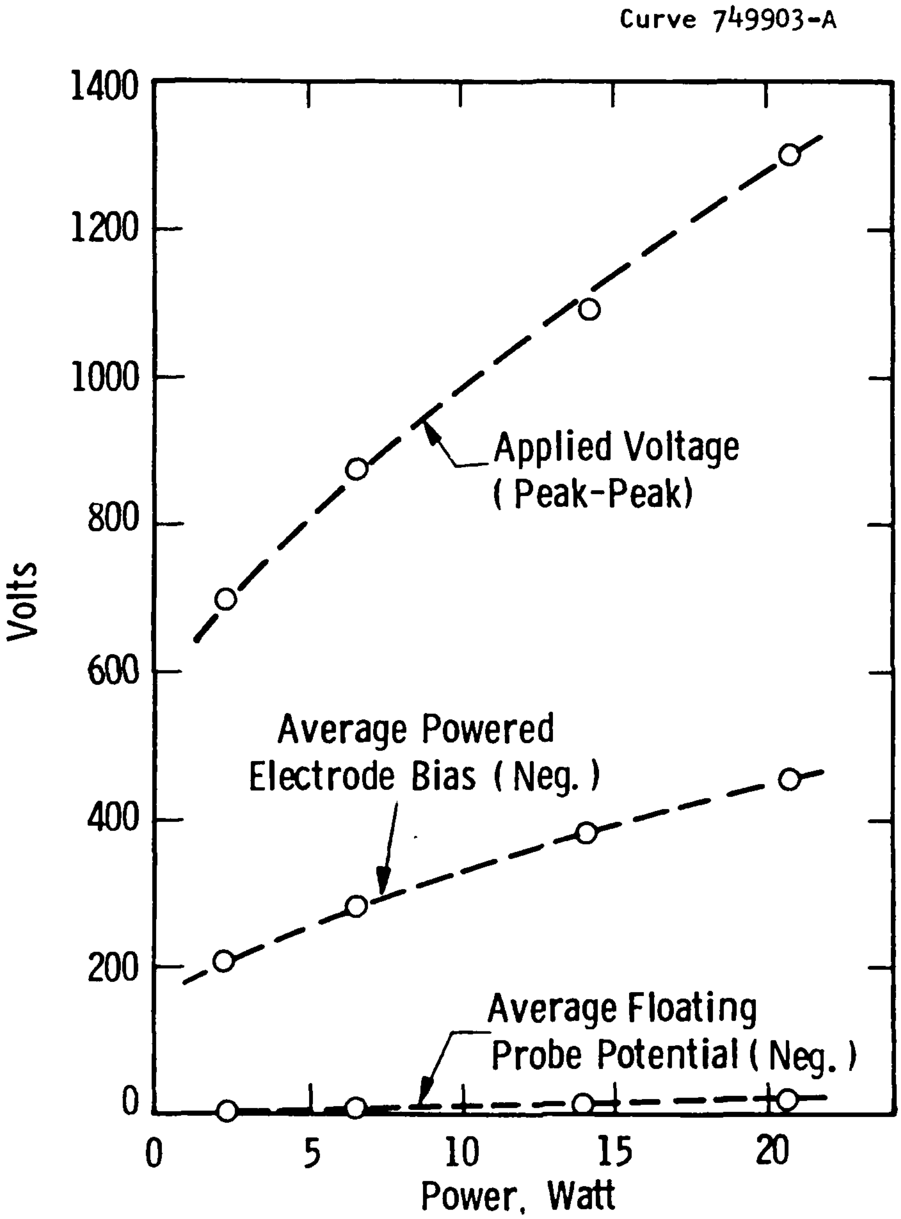

Figure 3.3 - Relations between average negative bias of the powered electrode, floating probe potential, and peak-to-peak plasma excitation voltage as a function of power.

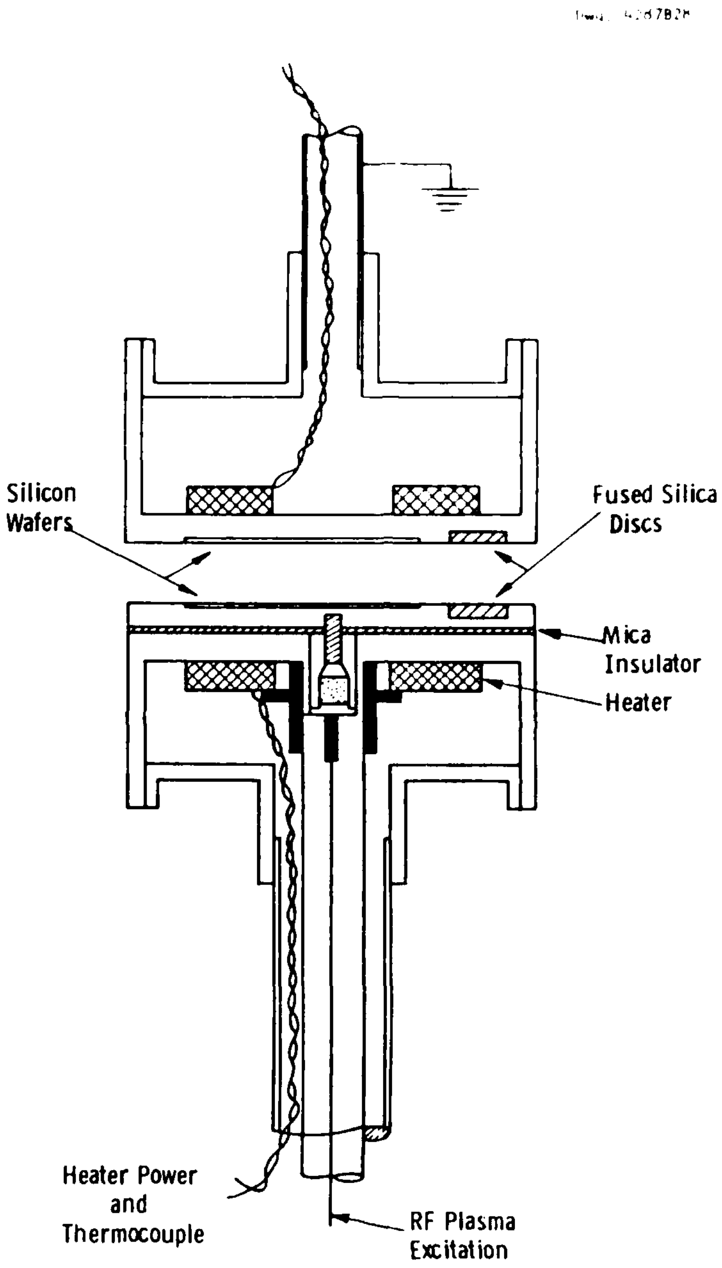

Figure 3.4 - Experimental deposition electrodes, showing positions of substrates.

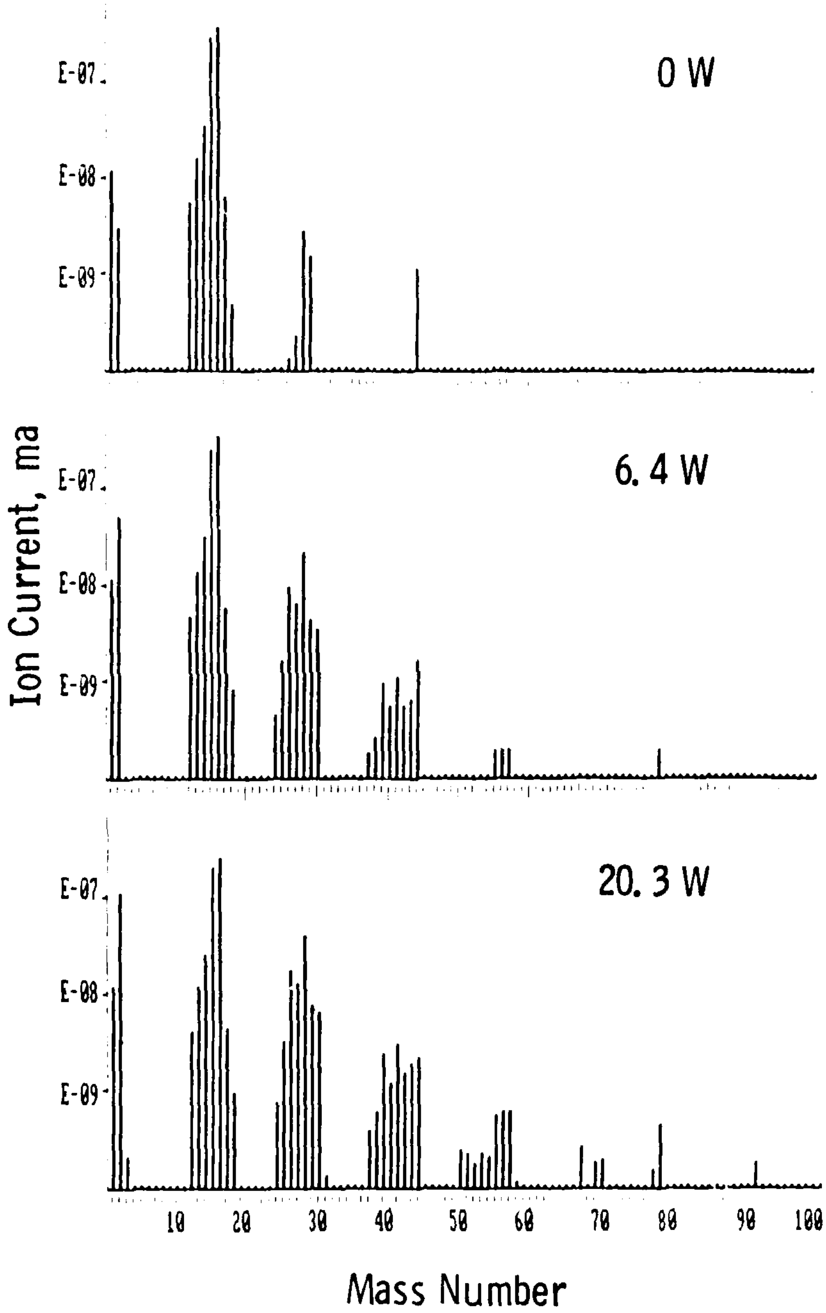

Figure 3.5 - Example of raw mass spectrometric data, taken downstream of the plasma, as a function of power.

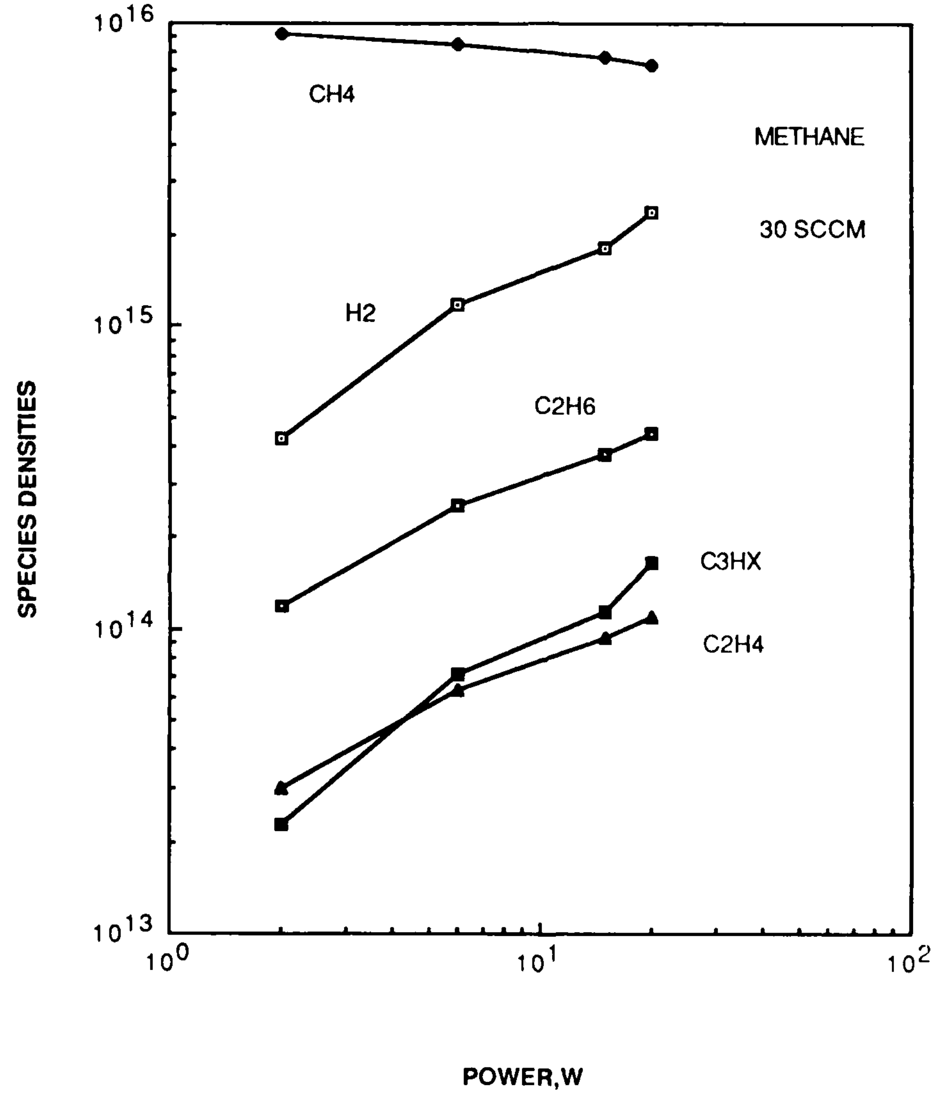

Figure 3.6 - Dependence of species densities versus power.

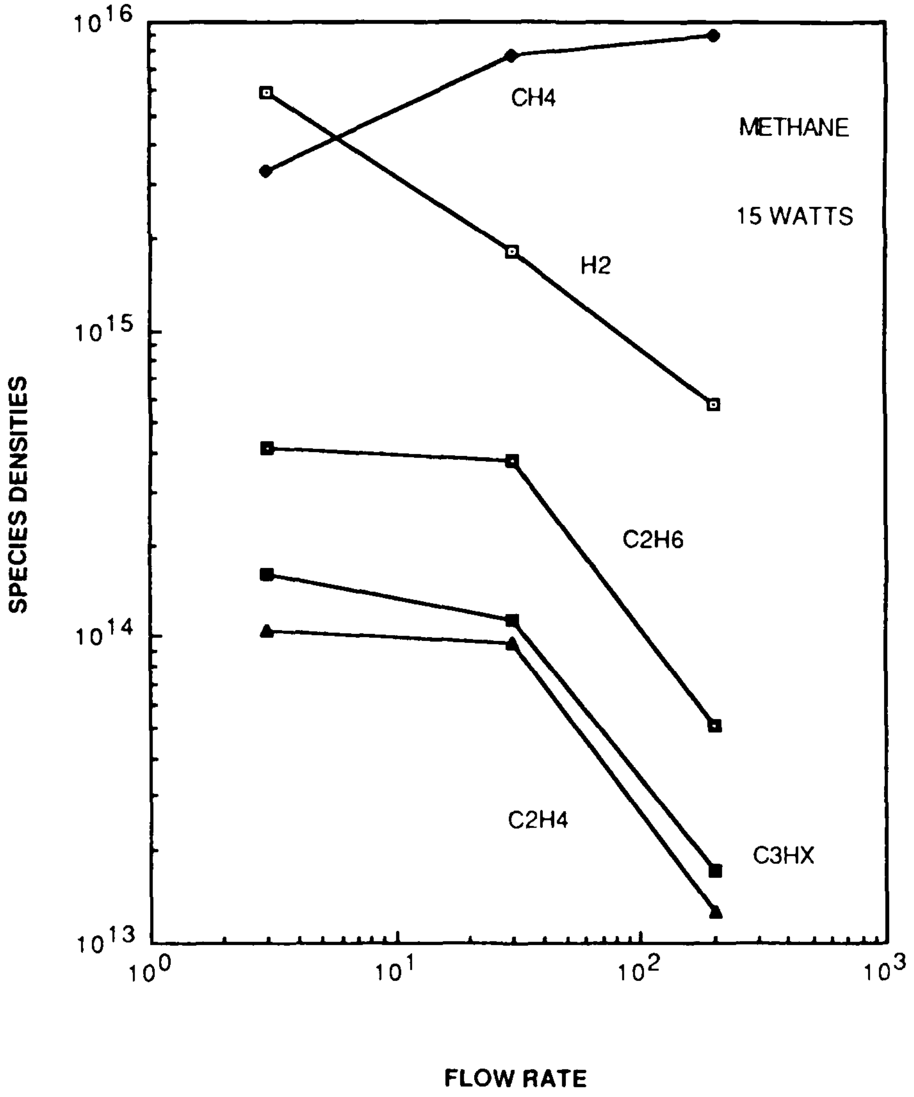

Figure 3.7 - Dependence of species densities versus flow rate.

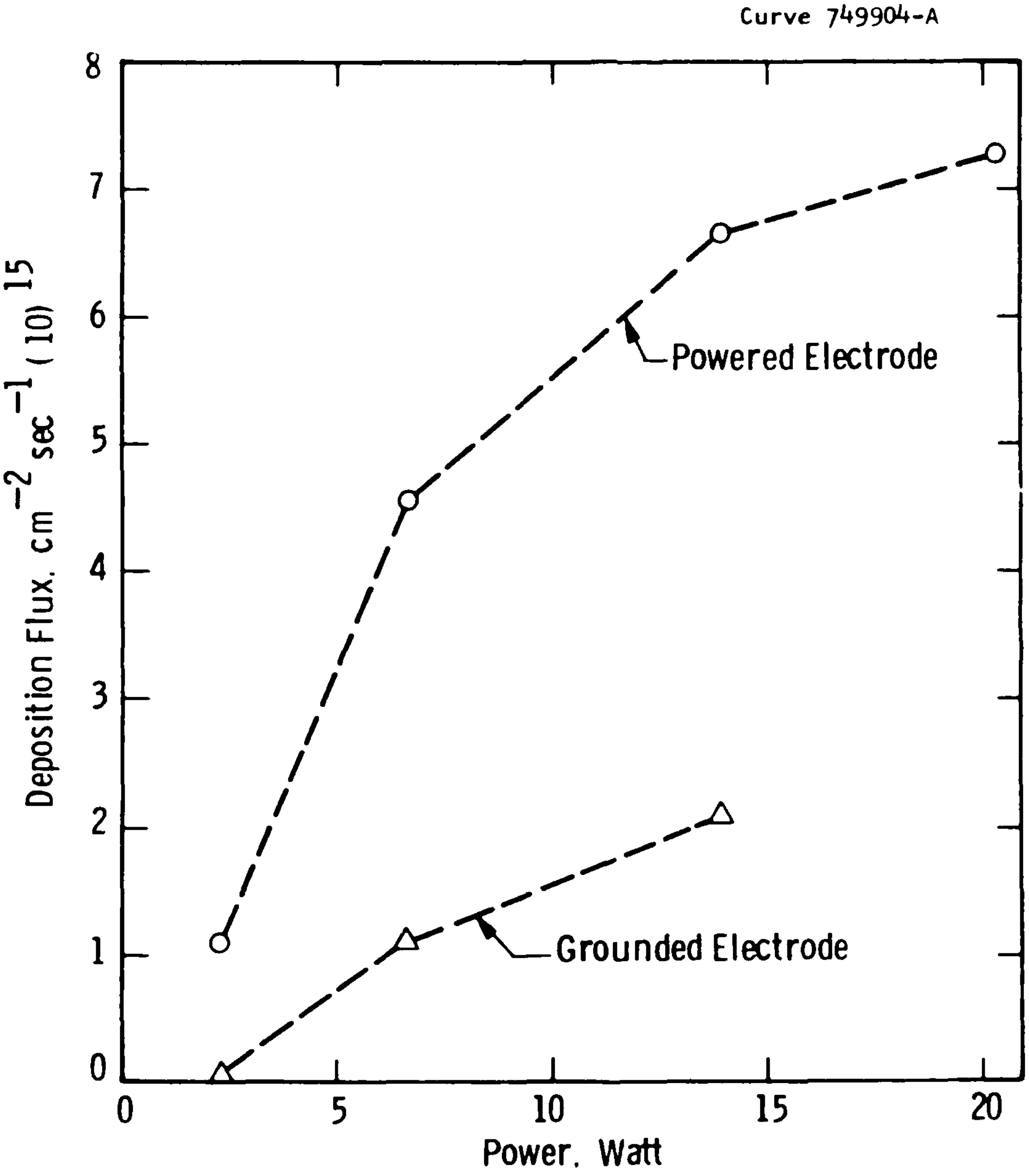

Figure 3.8 - Carbon deposition flux versus power at constant flow rate.

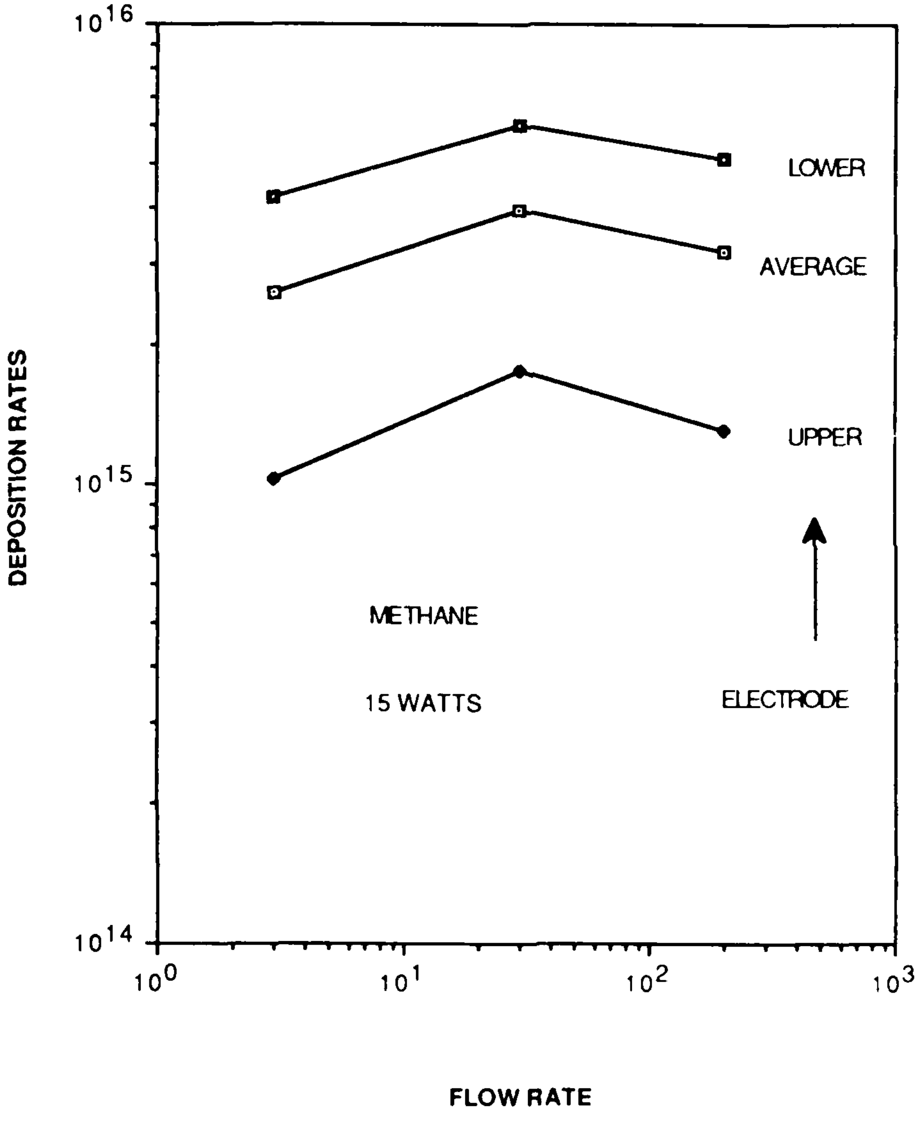

Figure 3.9 - Carbon deposition flux versus flow rate at constant power.

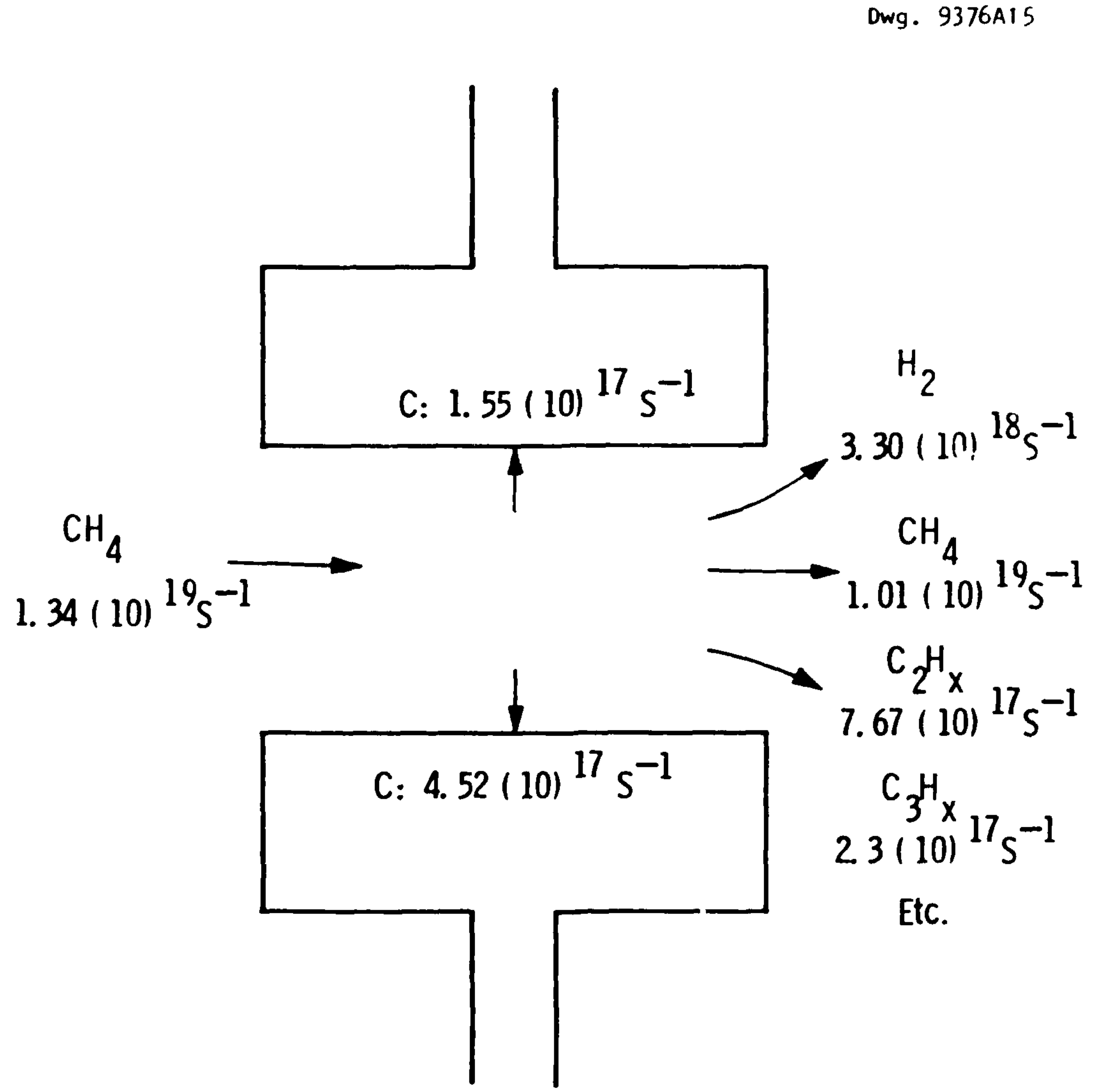

Figure 3.10 - Example of mass transport of carbon in the reactor at methane flow of 30sccm, power 15W.

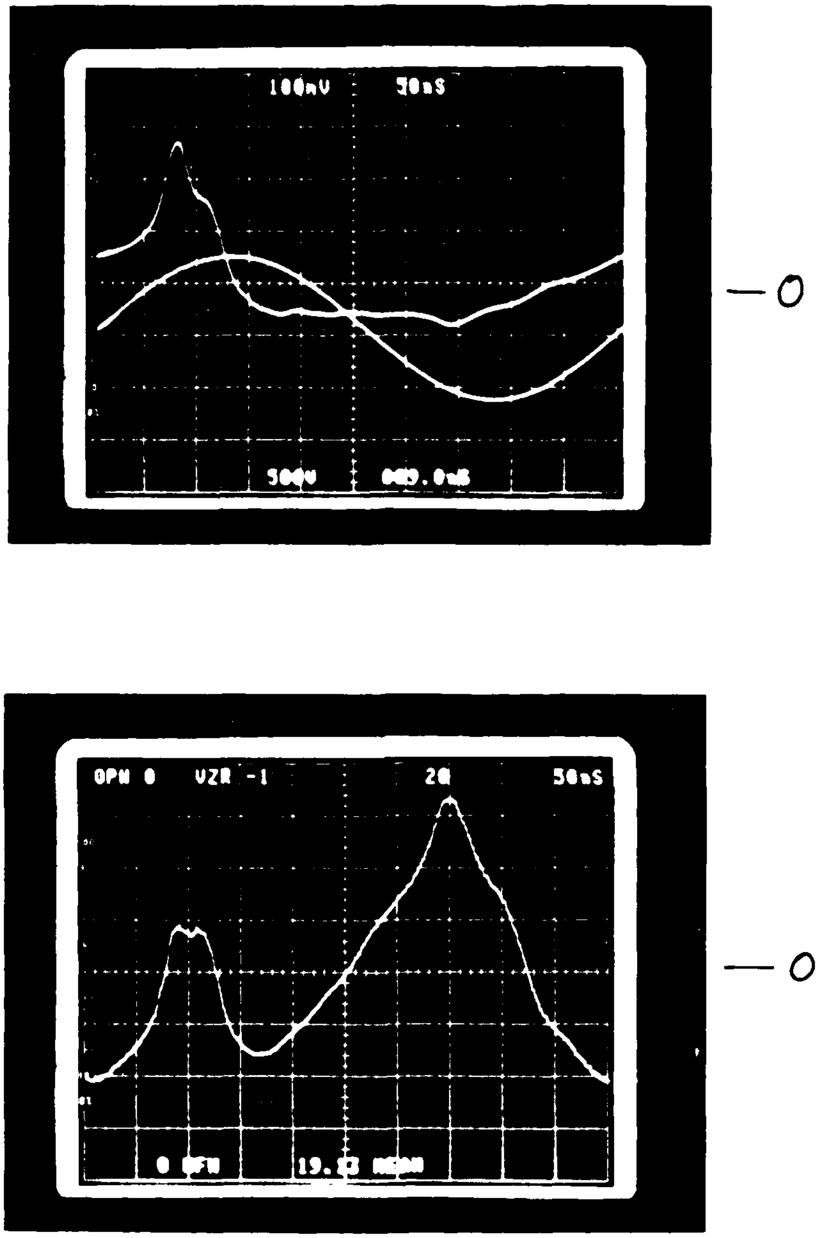

Figure 3.11 - Typical waveforms of the 2MHz plasma excitation. Upper photo: sinusiodal curve is voltage at 500V/cm, peaked curve is current at 100ma/cm. Lower photo: instantaneous power at 1W/cm.

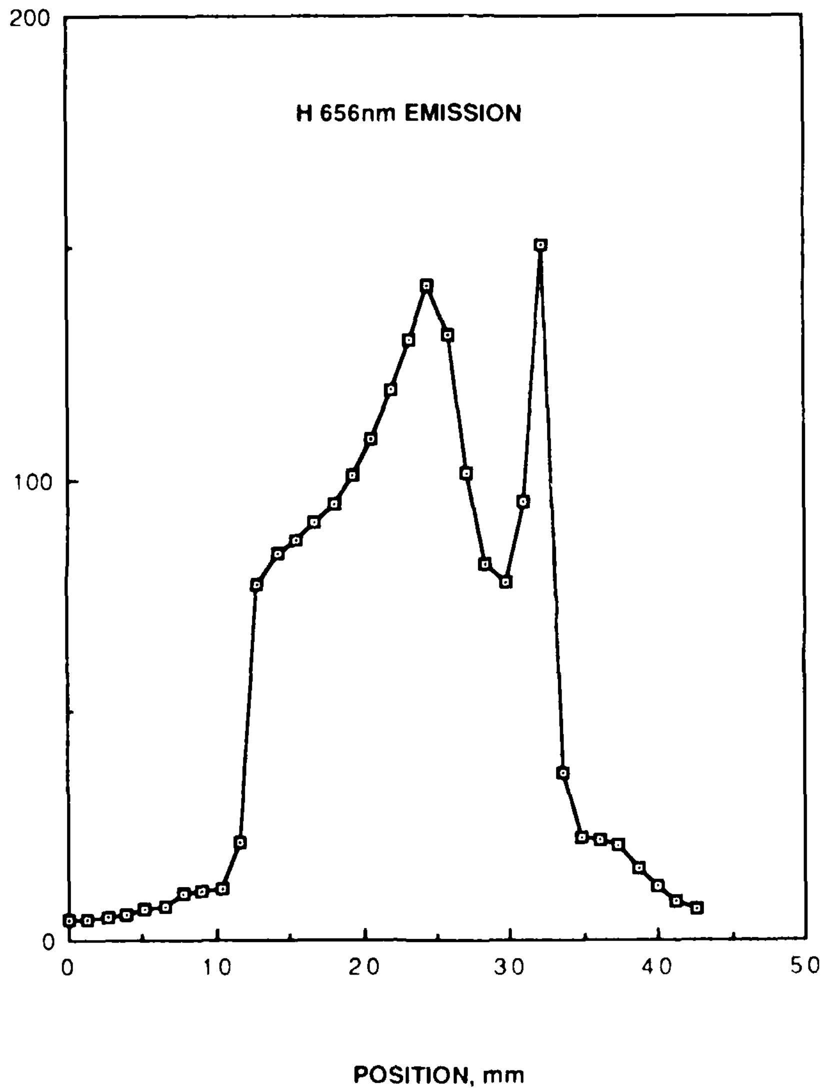

Figure 3.12 - Photocurrent of detector measuring relative radiance (radiant exitance) of the plasma as a function of position along the axis. Lower, powered electrode at 32mm, upper electrode at 12mm.

Curve 752806-A

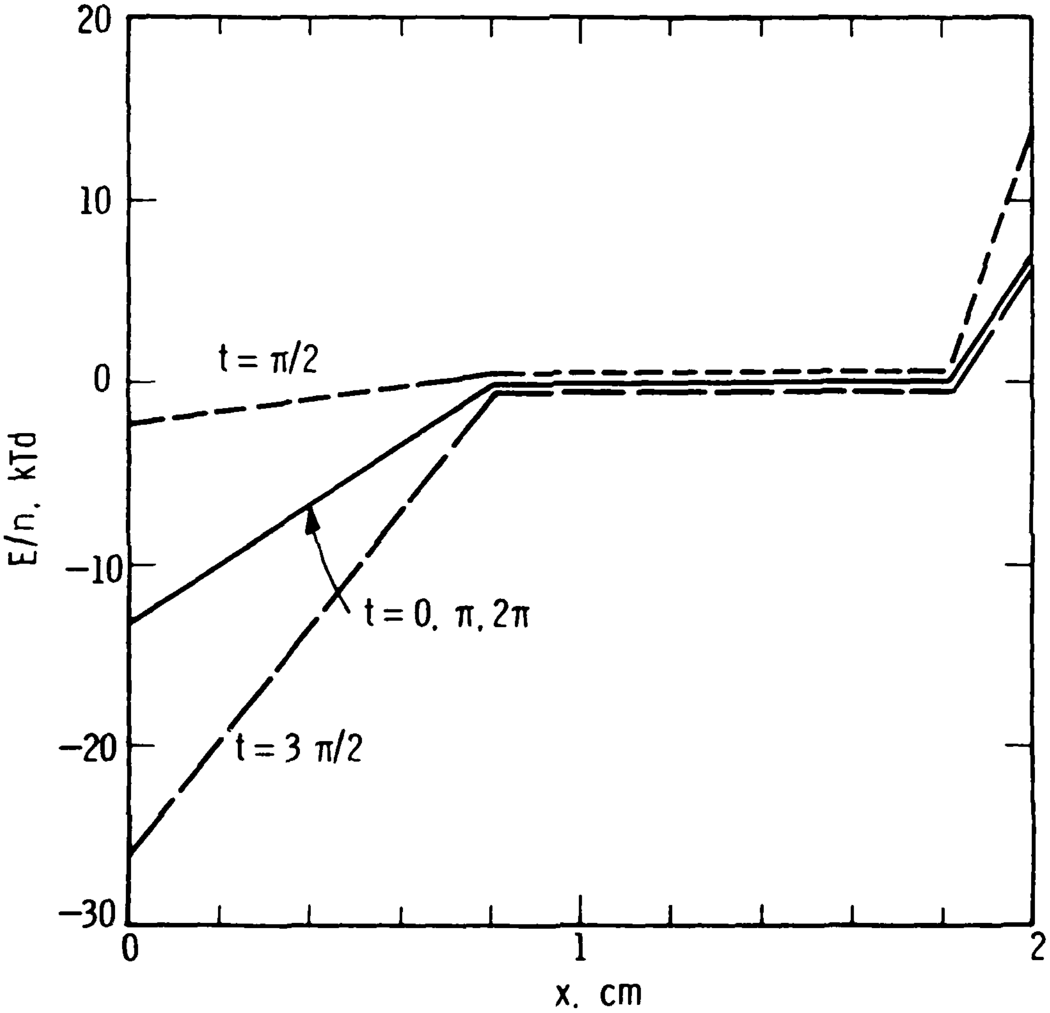

Figure 3.13 - Assumed E/n values (electric field to gas density ratio) versus position at several times within the RF cycle.

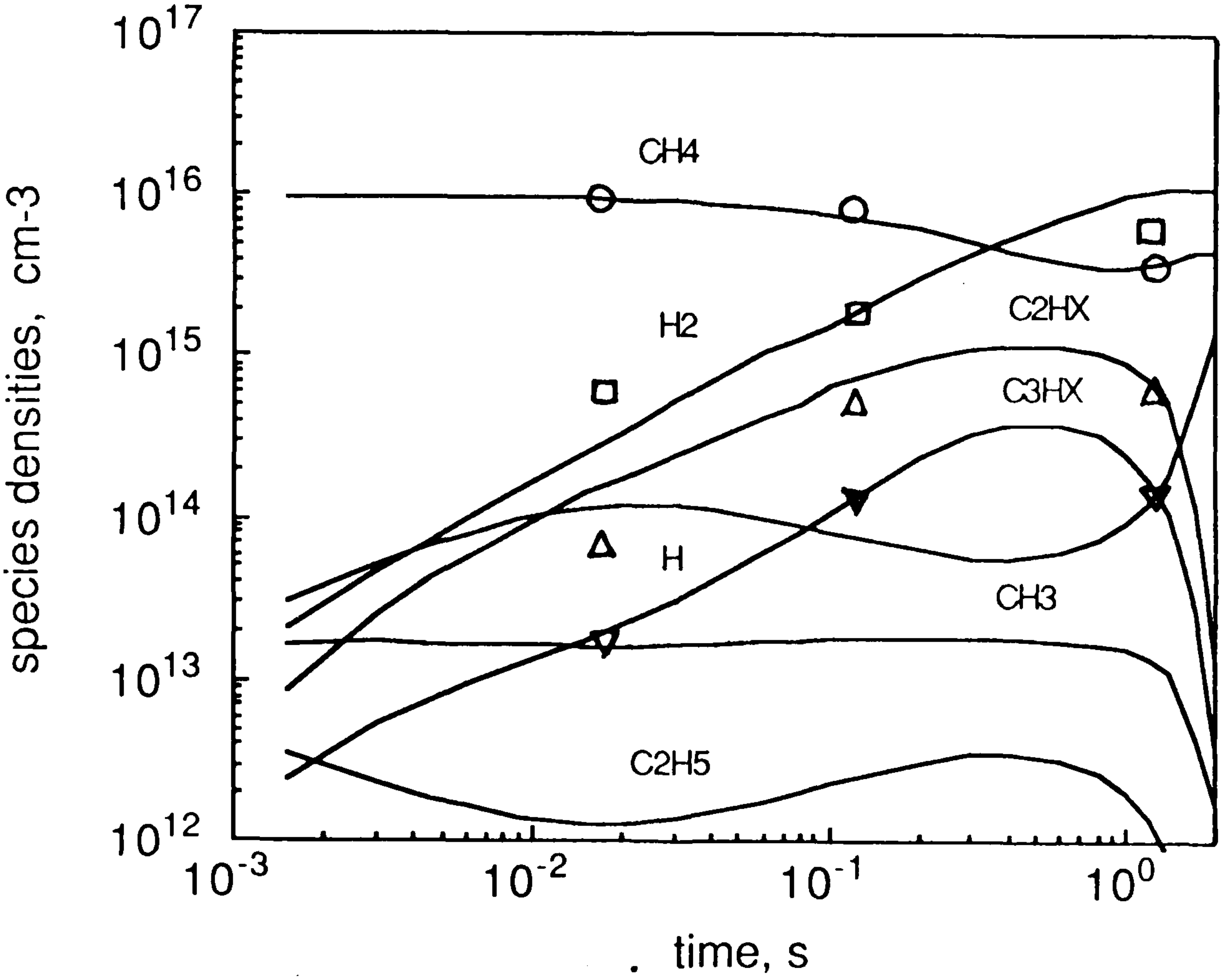

Figure 3.14 - Measured and predicted species densities versus time.

DOMINANT KINETIC PATHWAYS

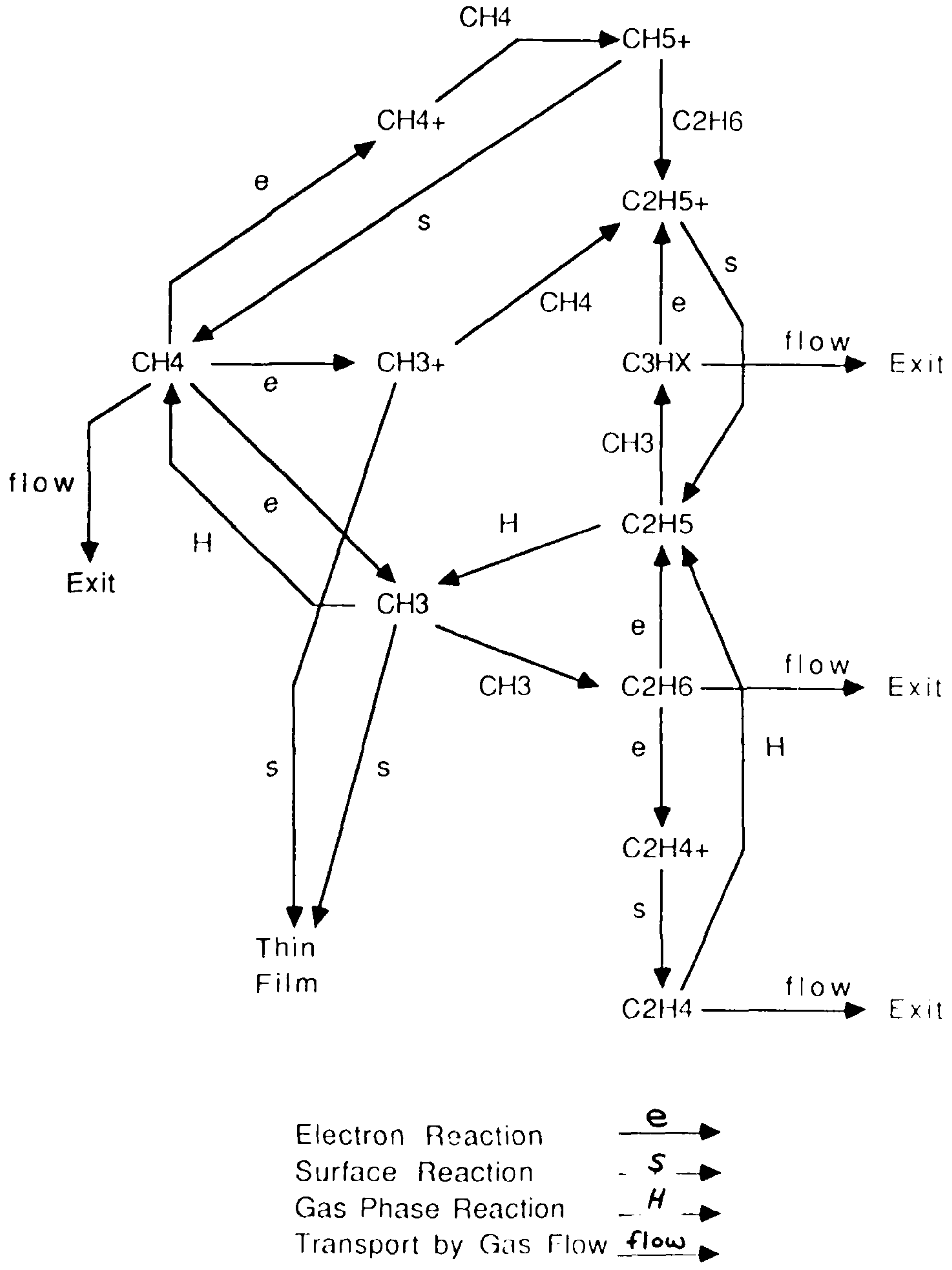

Figure 3.15 - Dominant kinetic pathways and species in methane plasmas.

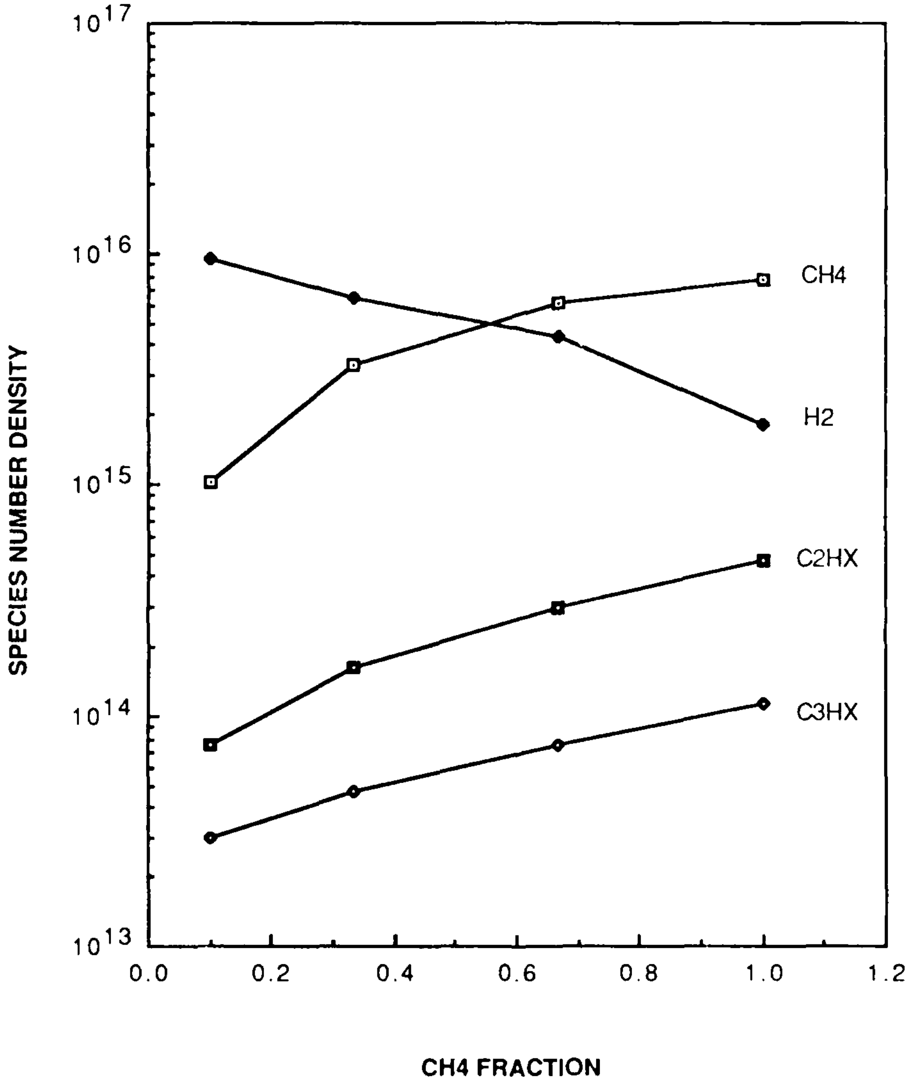

Figure 3.16 - Species densities versus methane concentration in methane-hydrogen plasmas, 30sccm, 15W.

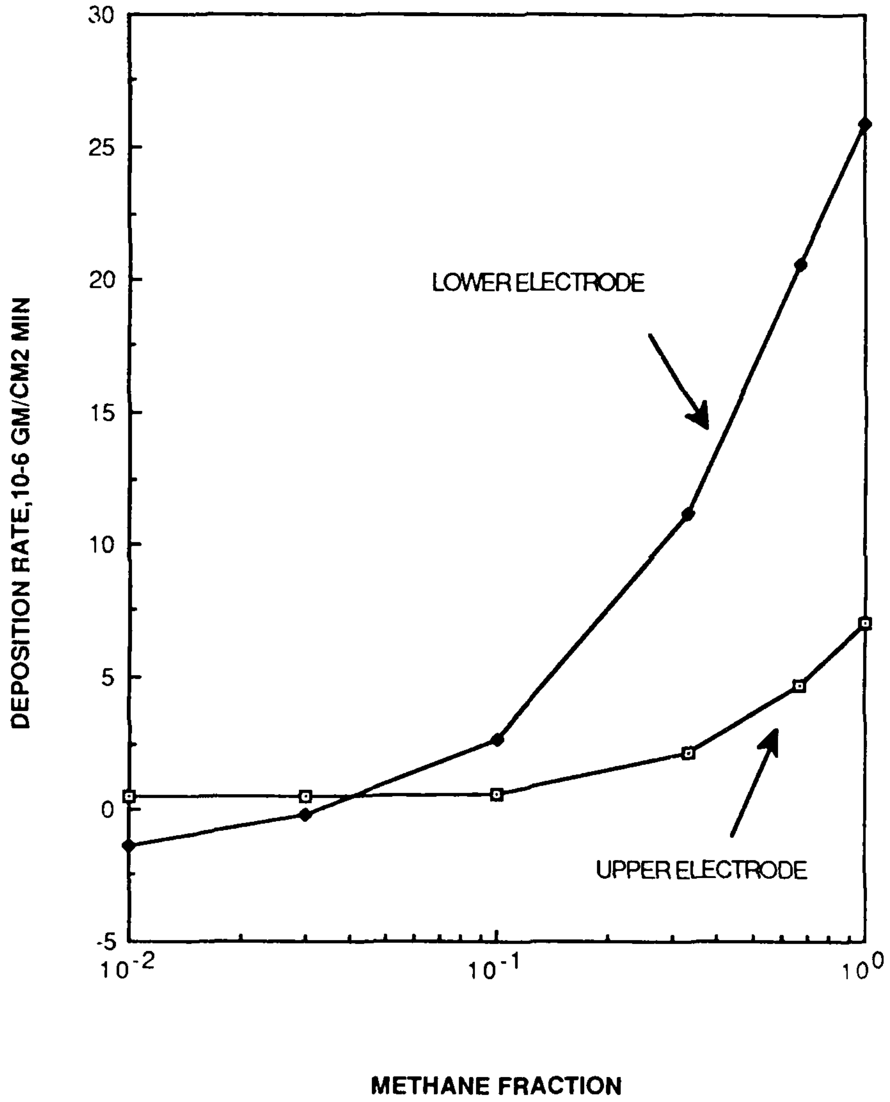

Figure 3.17 - Deposition rate versus methane concentration in methane-hydrogen plasmas, 30sccm, 15W.

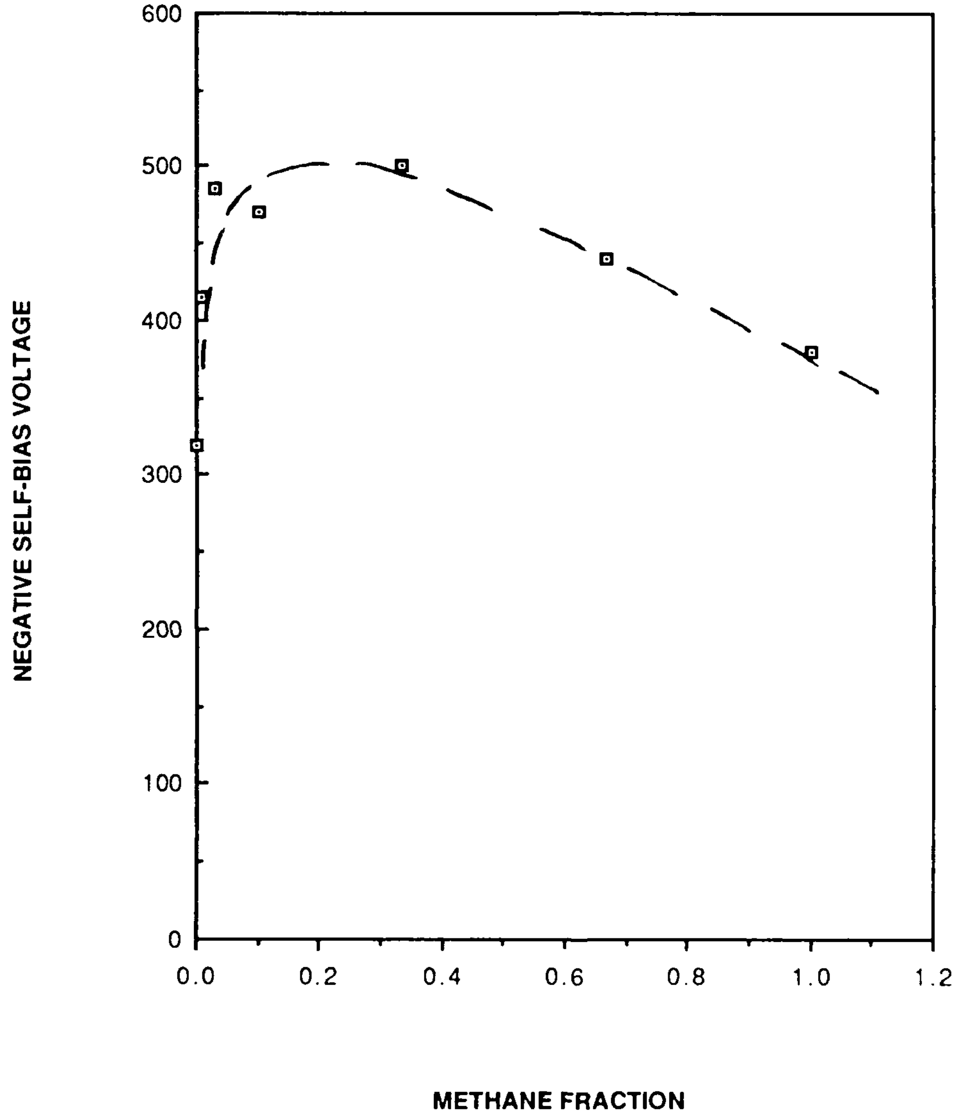

Figure 3.18 - Negative self bias voltage versus methane concentration in methane-hydrogen plasmas, 30sccm, 15W.

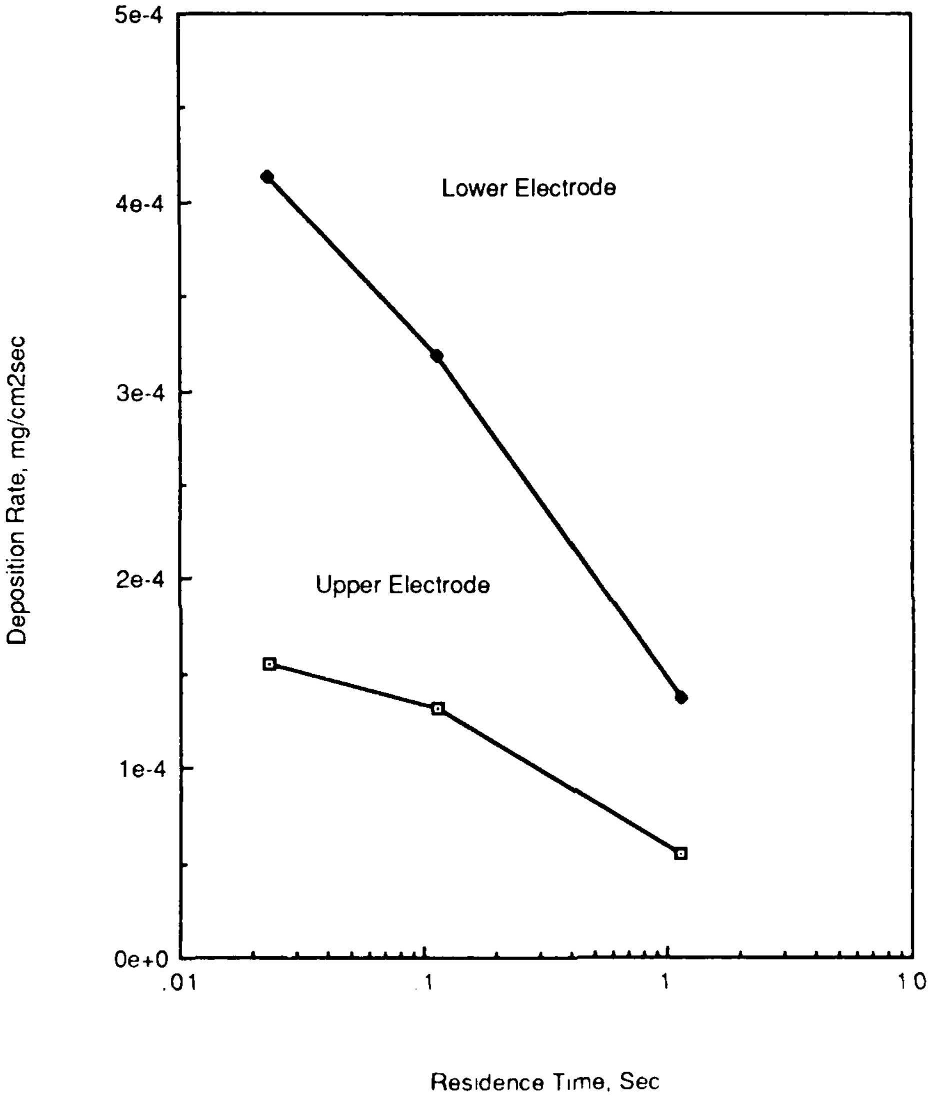

Figure 3.19 - Deposition rate versus gas residence time in methane-silane plasmas.

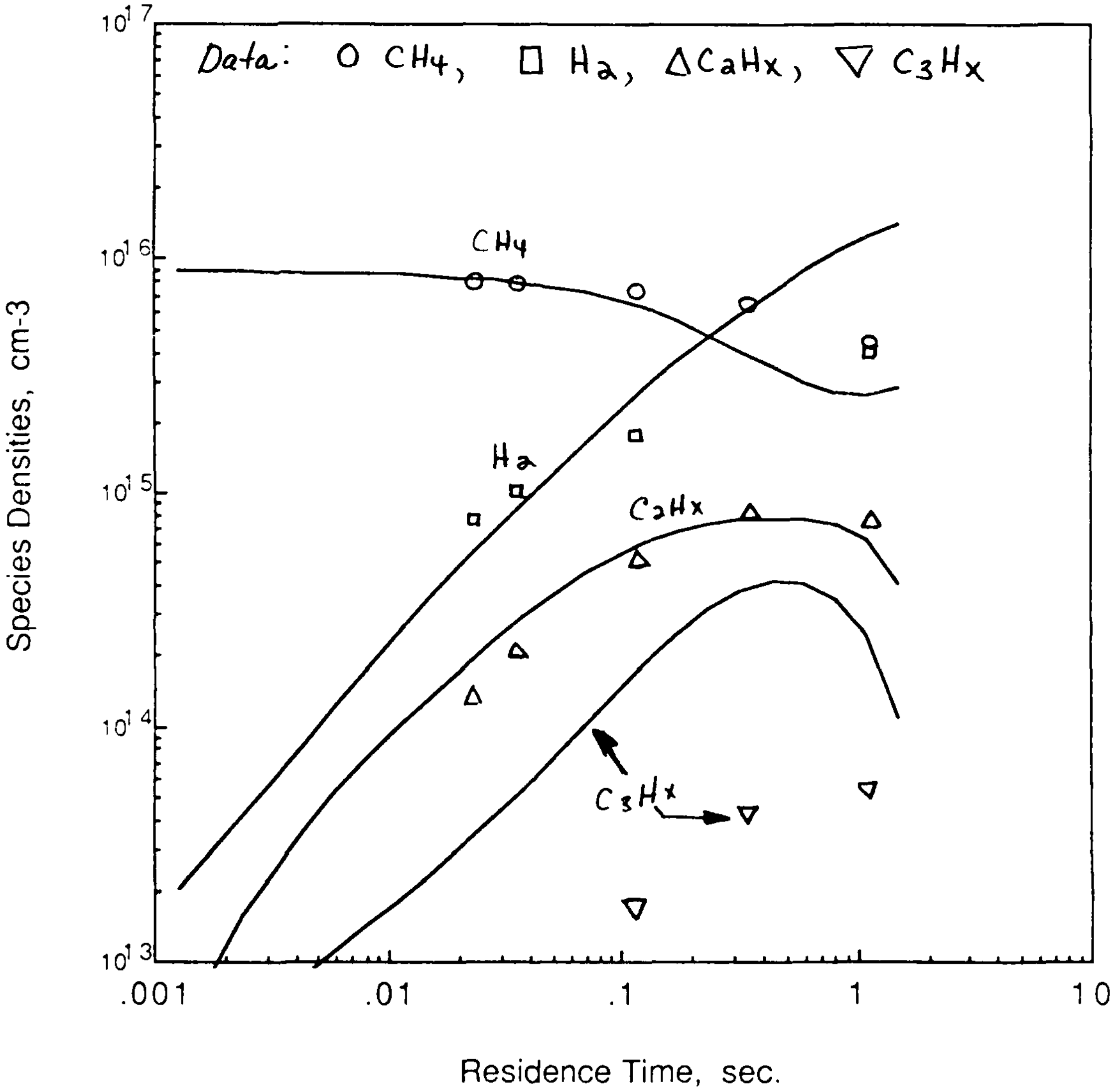

Figure 3.20 - Measured and predicted species densities versus gas residence time for hydrocarbons and hydrogen.

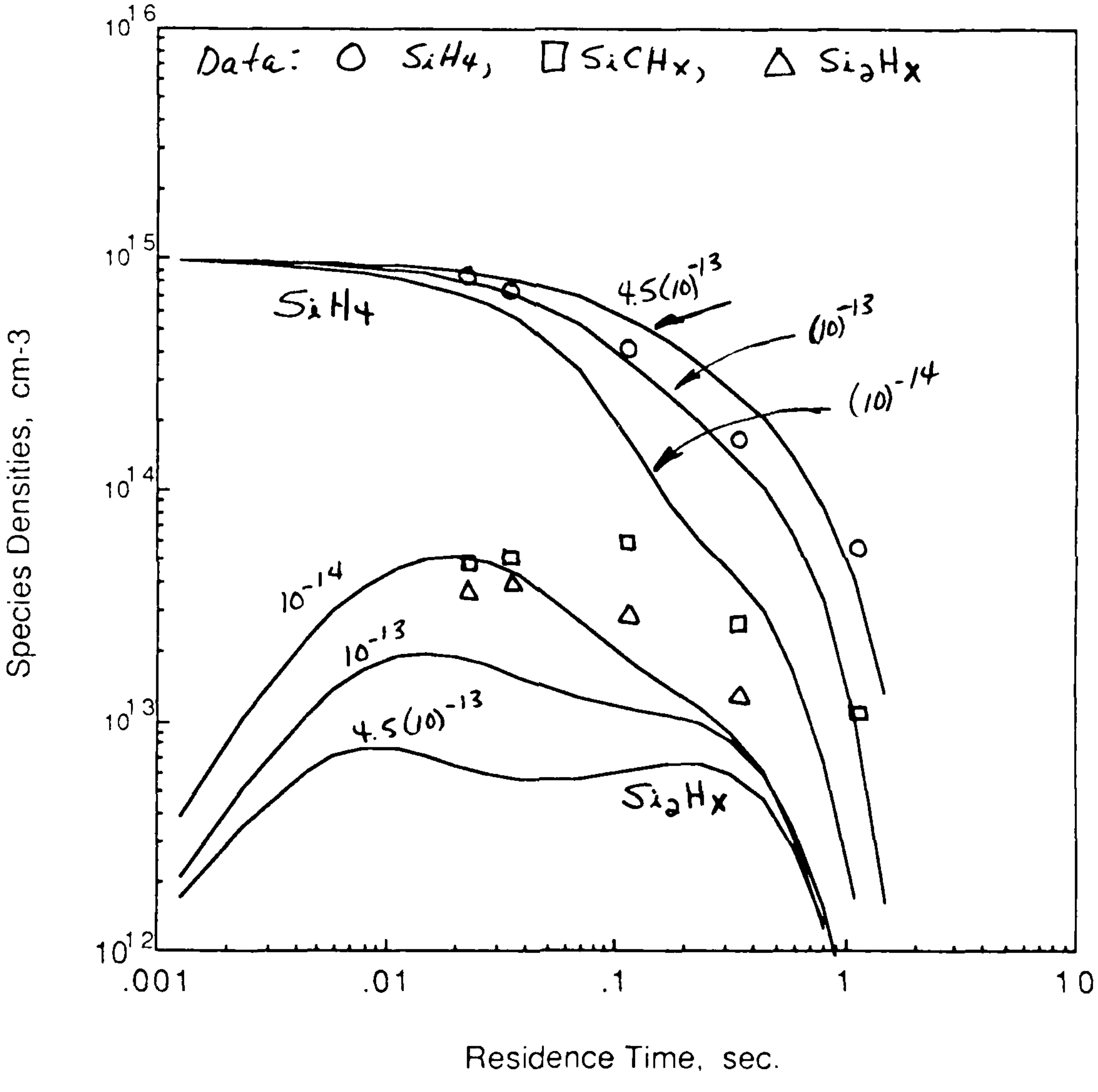

Figure 3.21 - Measured and predicted species densities for silicon-containing species versus residence time for several values of rate constant for the atomic hydrogen-silane reaction.

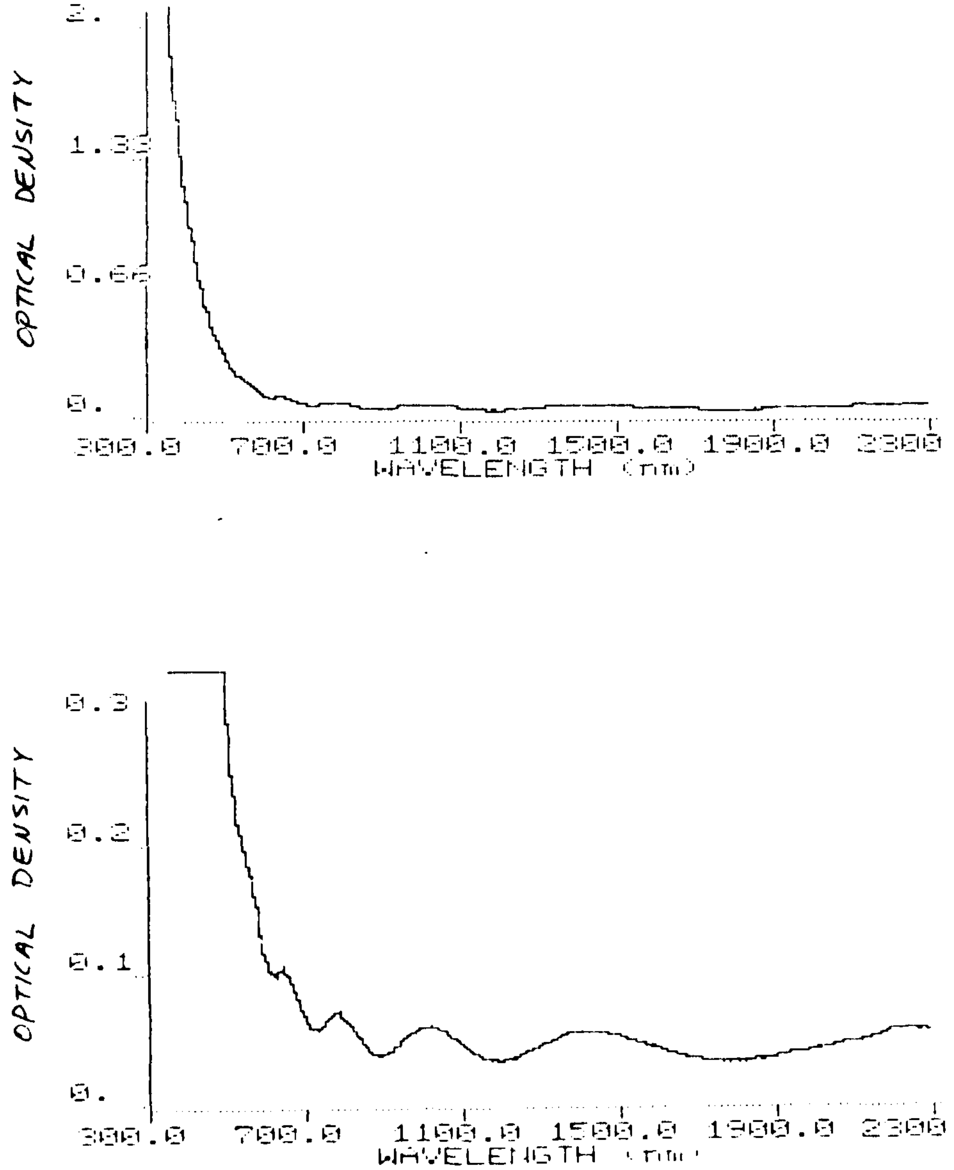

Figure 4.1 - Measured optical density versus wavelength for a hydrogenated carbon film deposited from a methane plasma.

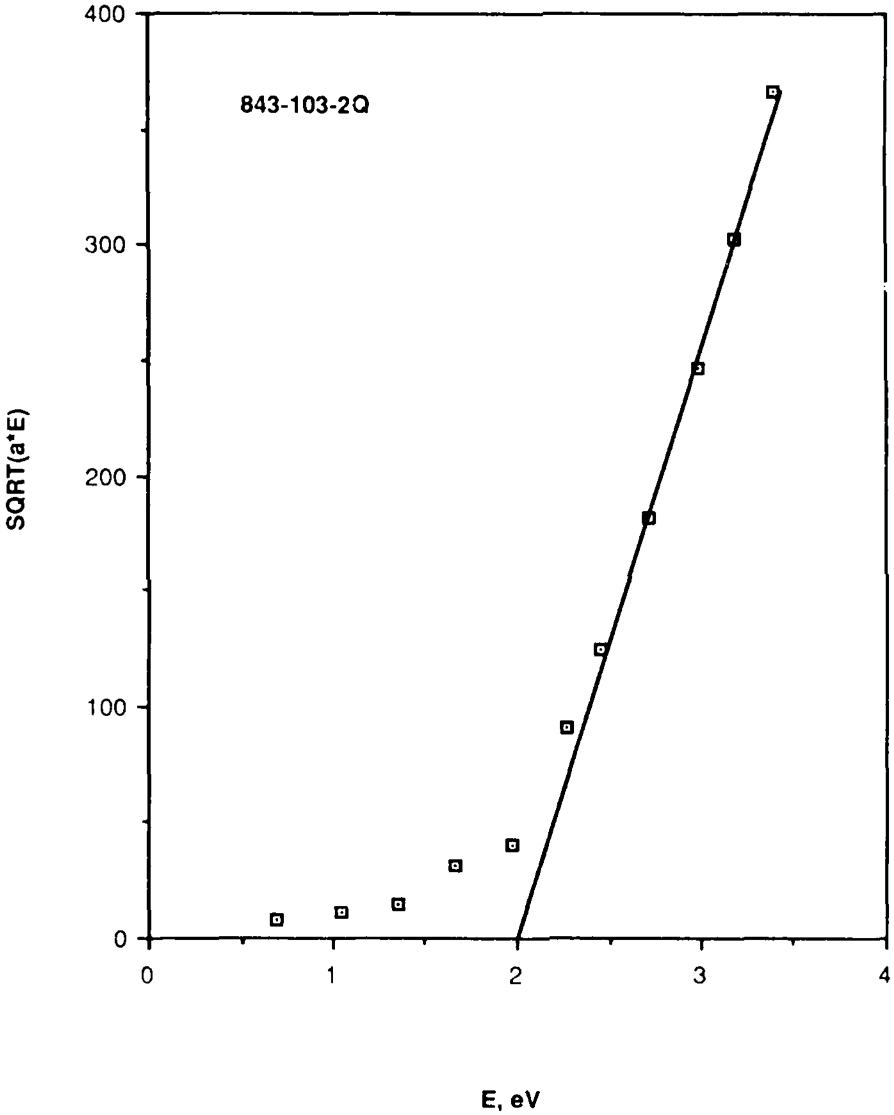

Figure 4.2 - Tauc plot of the data of Fig. 4.1 with an extrapolation of the straight part of the curve to estimate the optical gap.

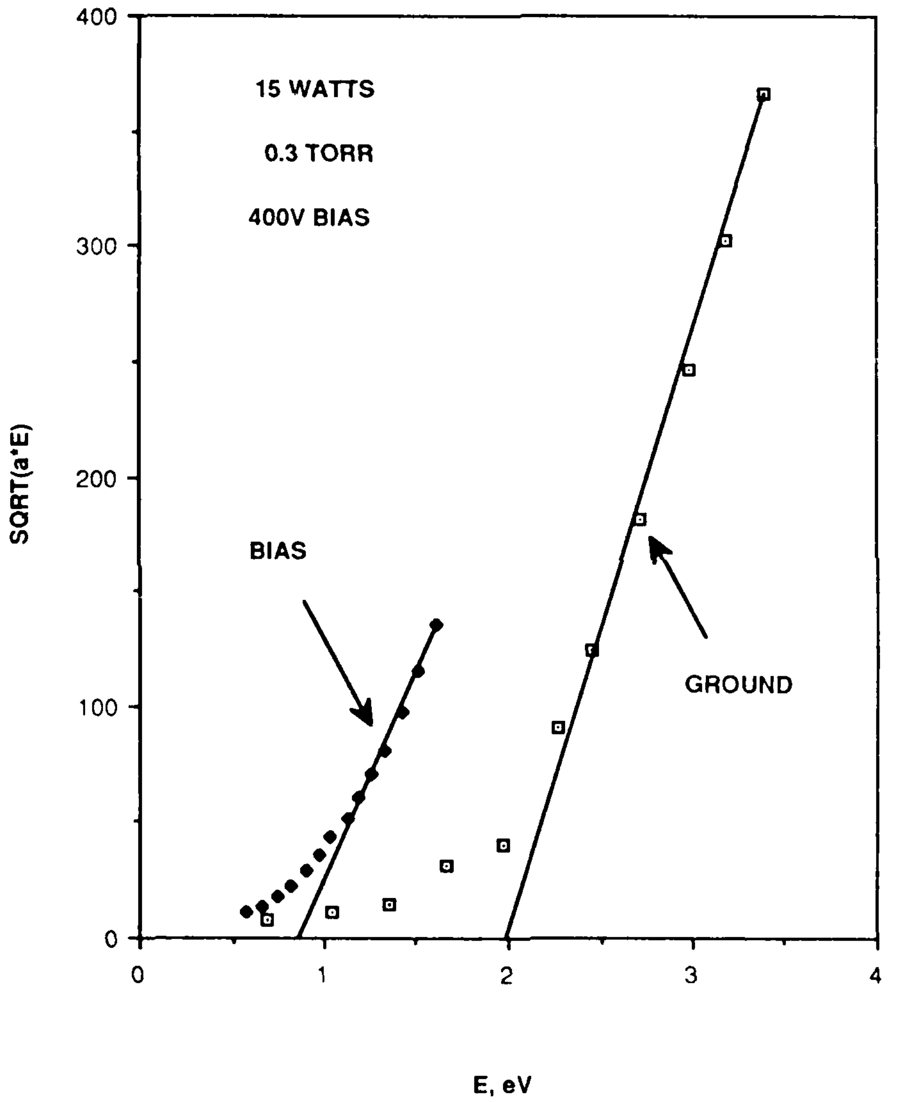

Figure 4.3 - Tauc plots for films deposited on the biased (powered) electrode and the grounded electrode of a methane plasma.

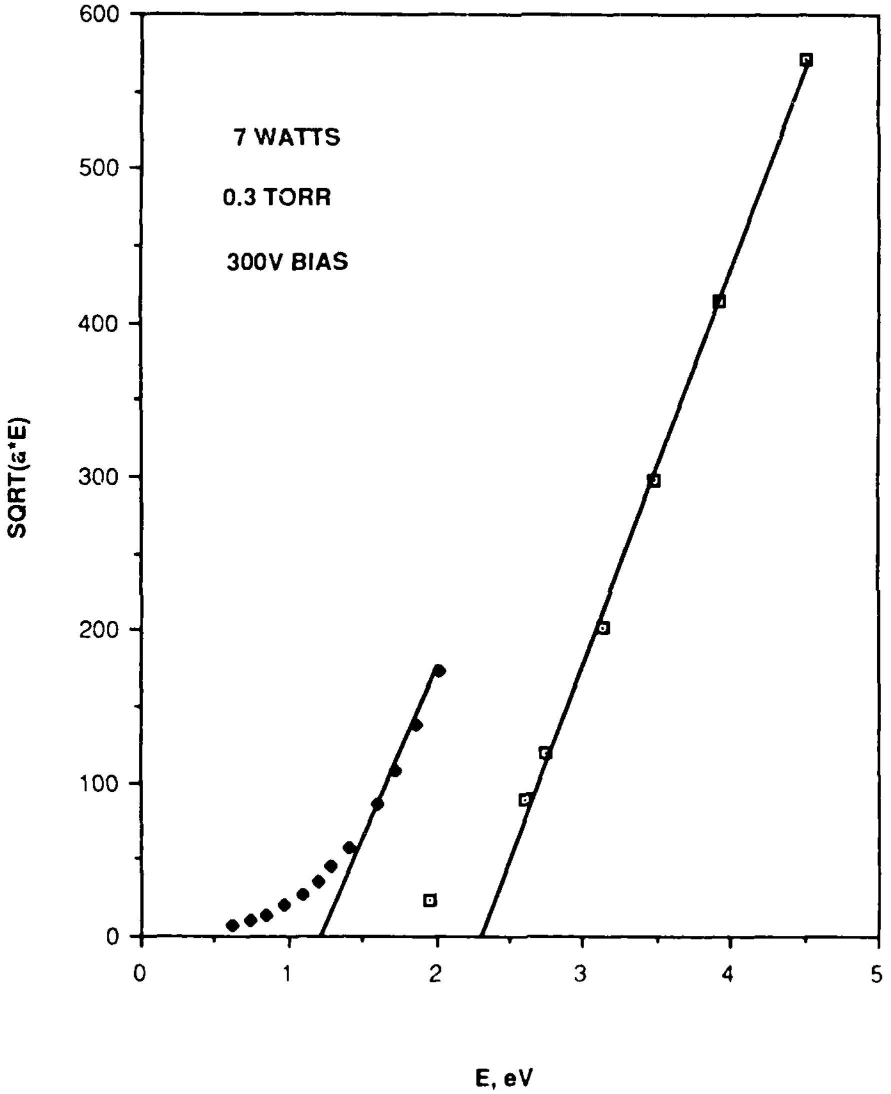

Figure 4.4 - Tauc plots, to be compared to Fig. 4.3, showing the influence of plasma power on the optical gaps of the films.

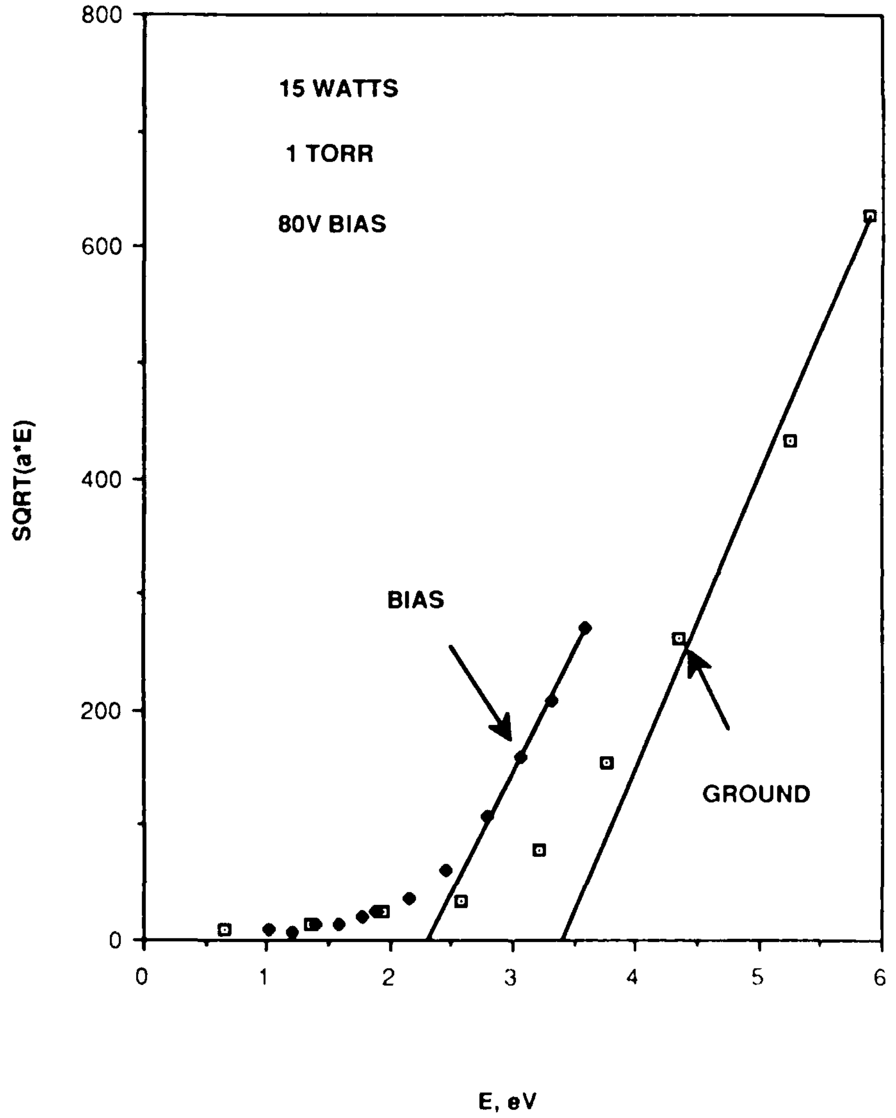

Figure 4.5 - Tauc plots, to be compared to Fig. 4.3, showing the influence of pressure on the optical gaps of the films.

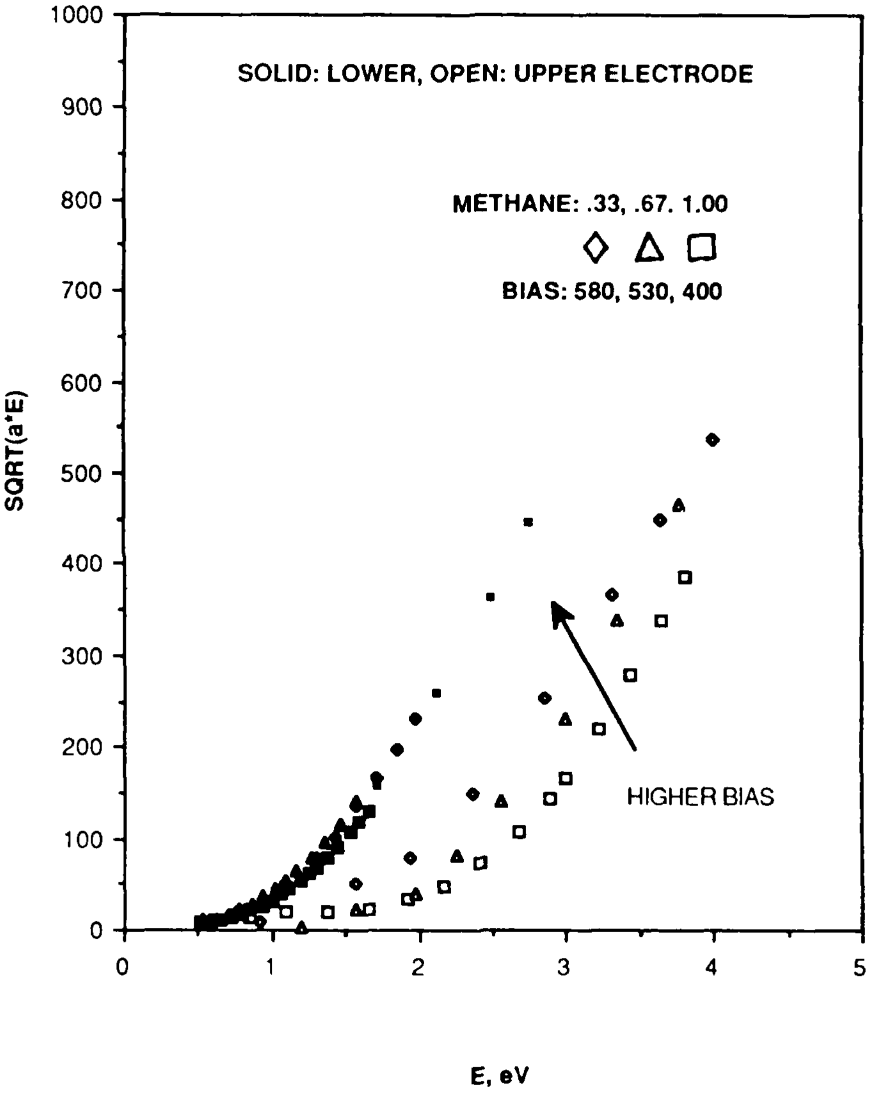

Figure 4.6 - Tauc plots for films deposited from methane-hydrogen plasmas with several different concentrations of methane.

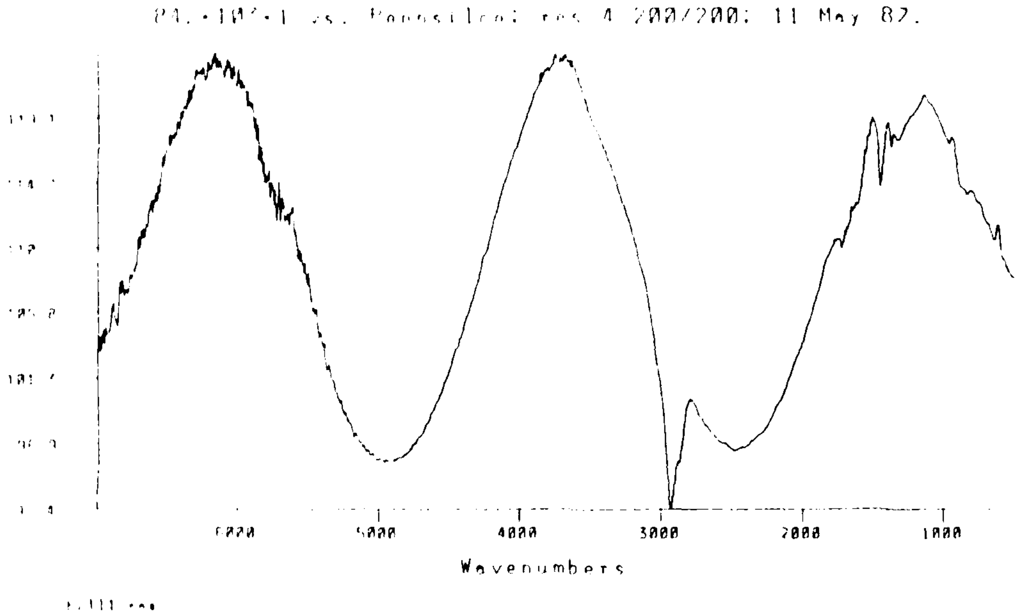

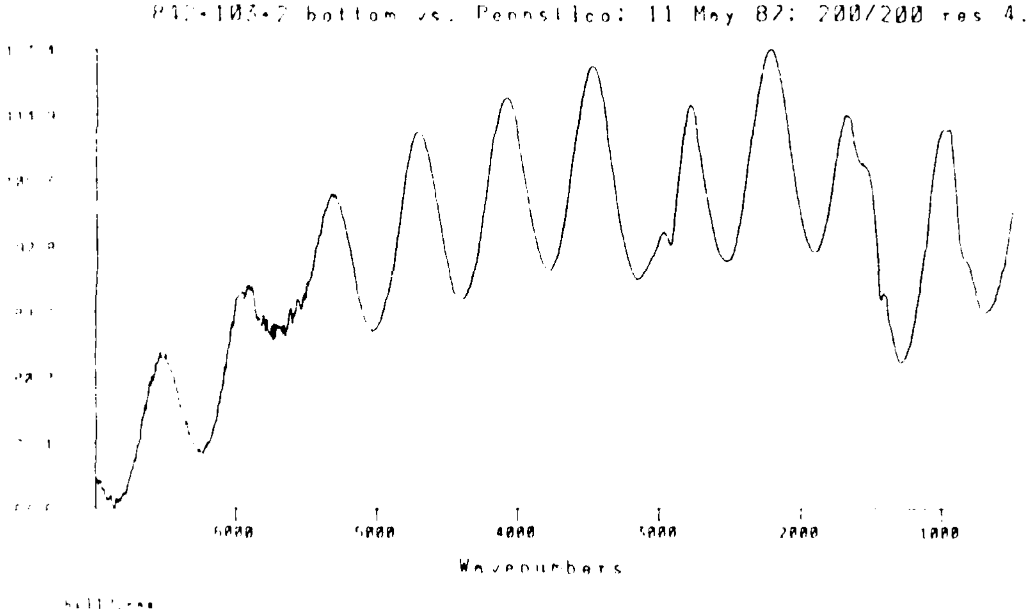

Figure 4.7 - Infrared spectra of samples from the grounded electrode (upper trace) and biased electrode (lower trace) of a methane plasma. Data taken prior to exposure of the films to air.

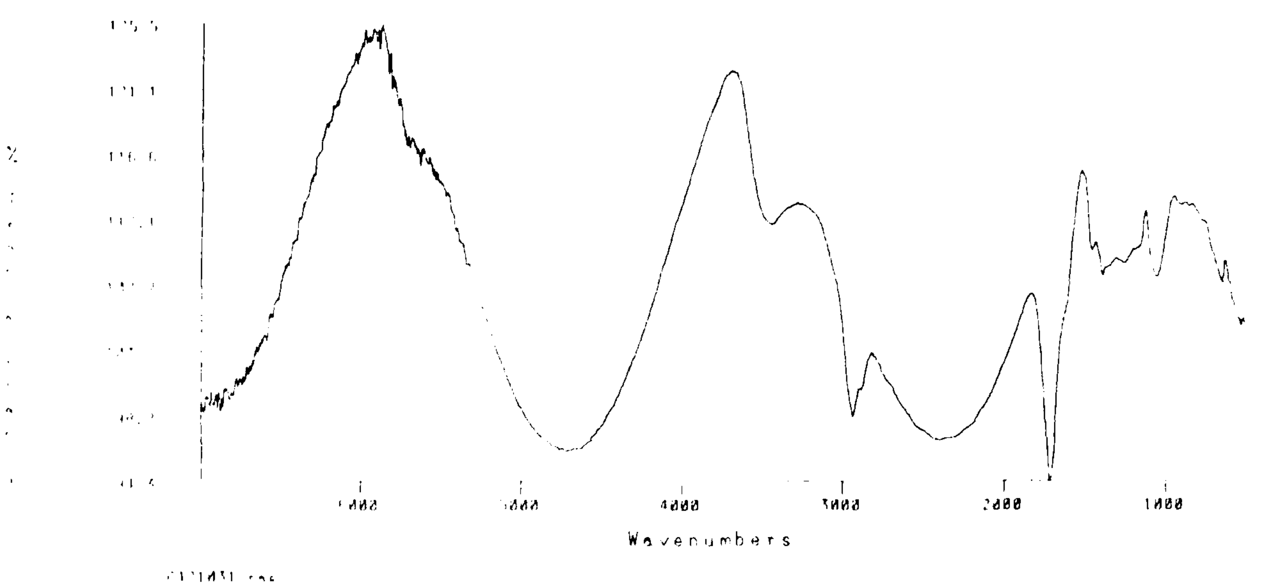

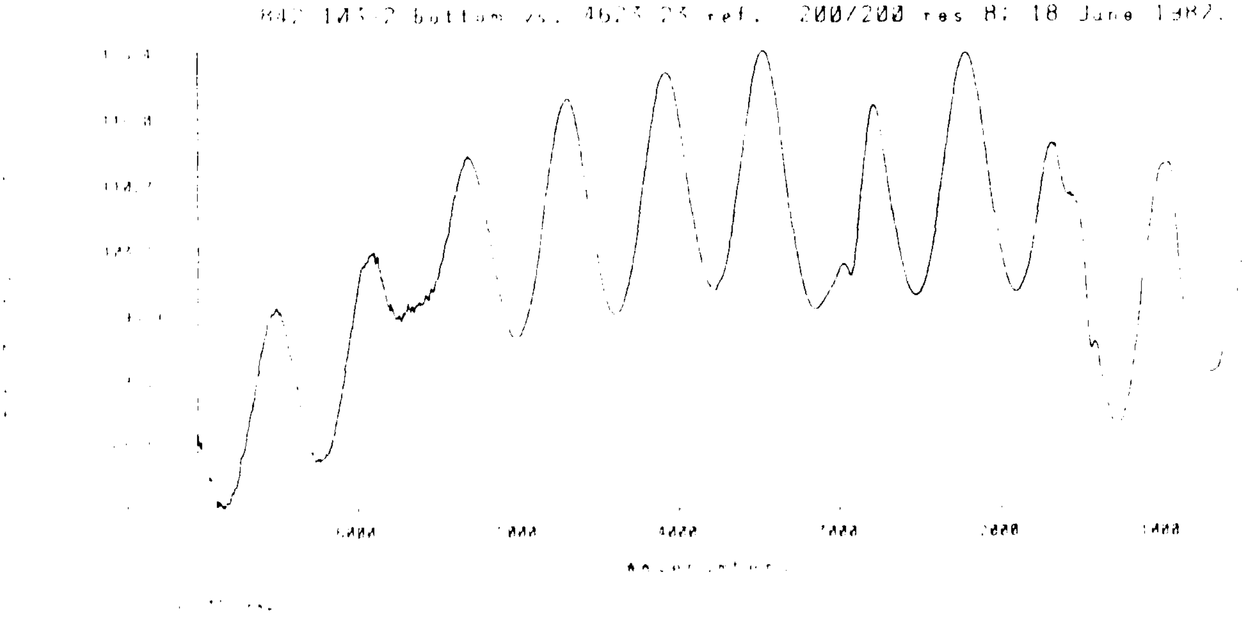

Figure 4.8 - Infrared spectra of the films of Fig, 4.7 taken after five weeks exposure to air, showing reaction of the film from the grounded electrode.

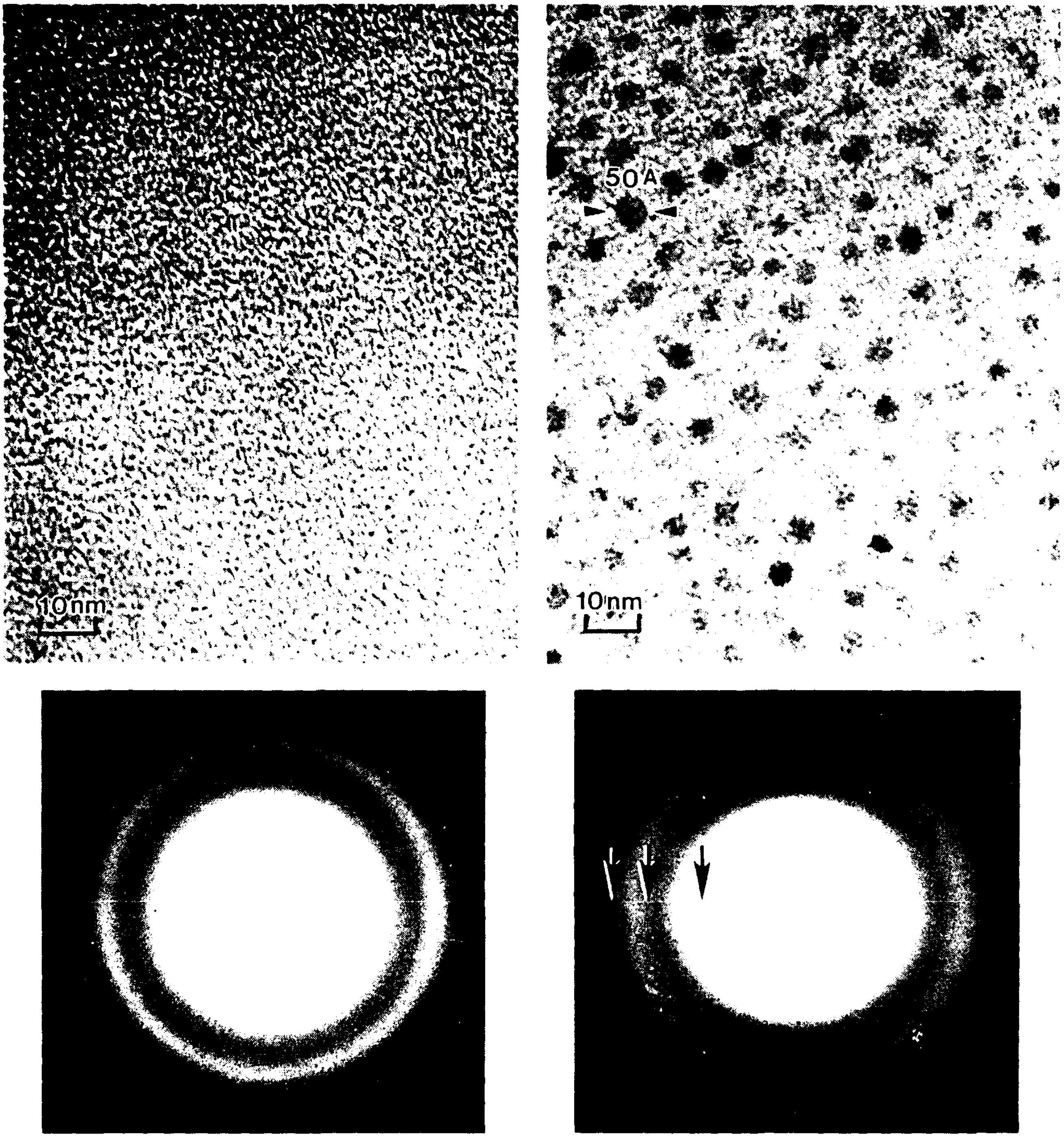

Figure 4.9 - TEM microphotos of films from the grounded electrode (left) and the powered electrode (right) of a methane plasma. Respective electron diffraction patterns are shown below the photos.

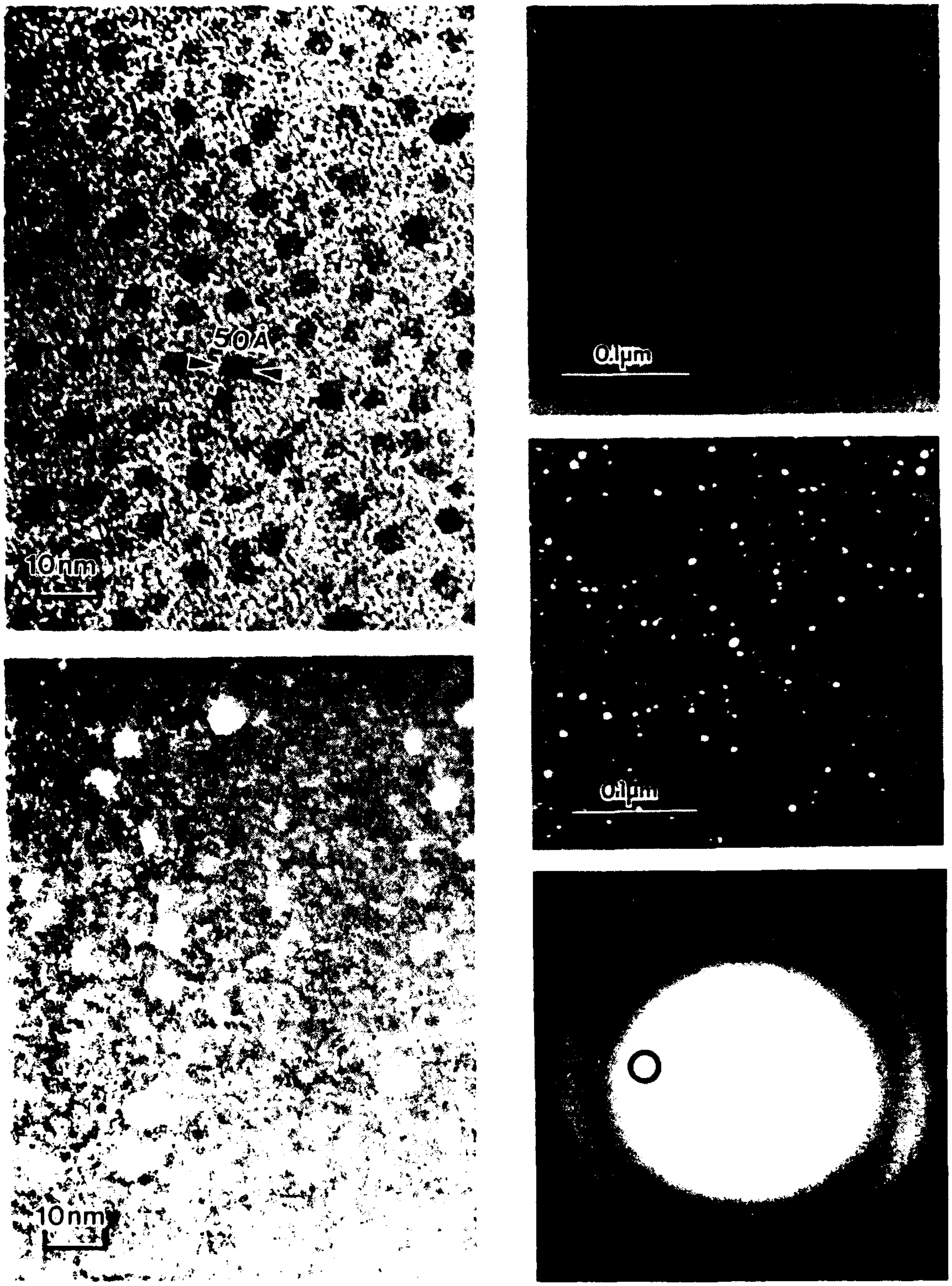

Figure 4.10 - In the left column light and dark field TEM microphotos are shown of a film from the biased electrode of a methane plasma. The lower right photo shows the position in the diffraction pattern that was selected to produce the dark field photo. Photos with lower magnification are shown above the diffraction pattern.

Apparatus Used to Study Semiconductor Surface Chemistry

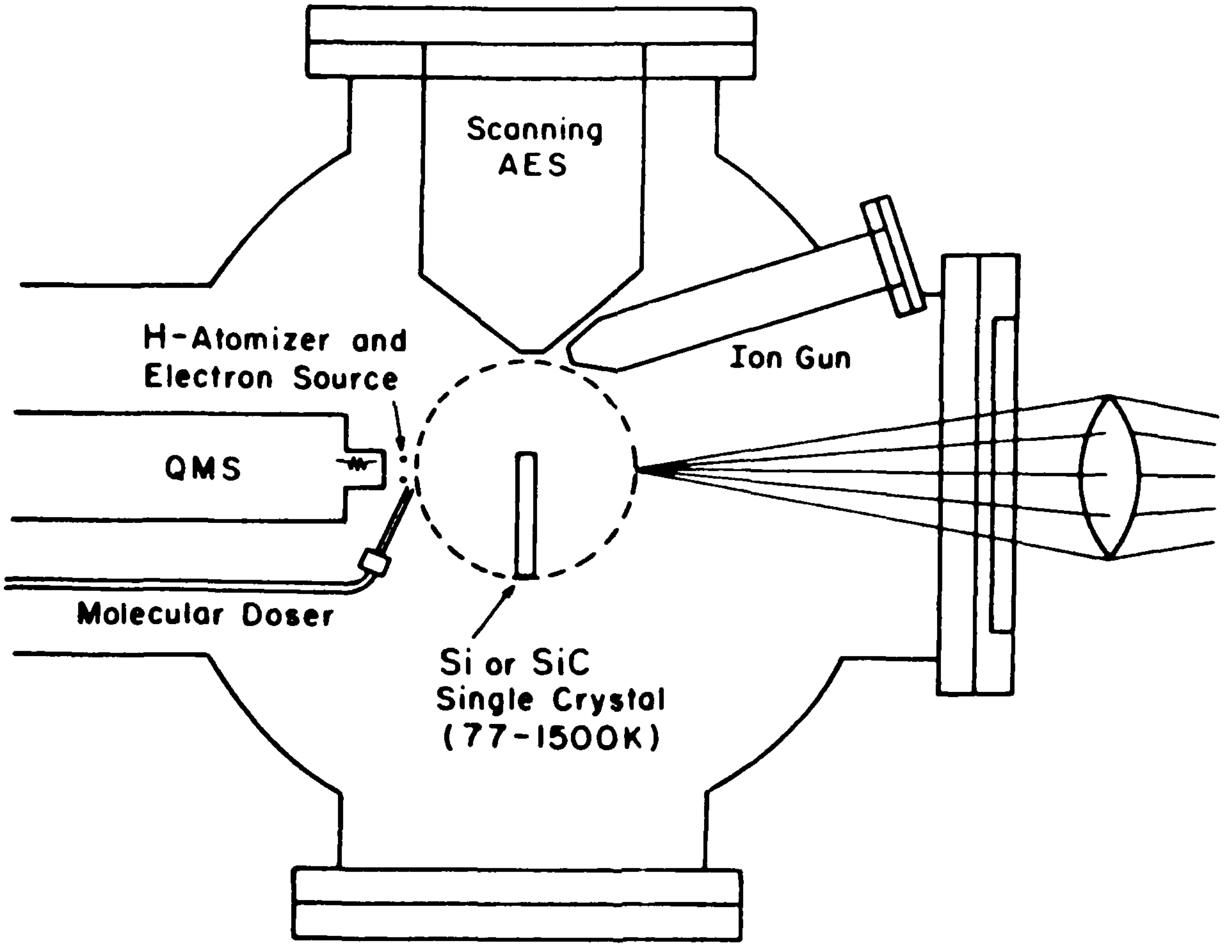

Figure 5.1

Mounting Scheme for Si Single Crystal Specimens

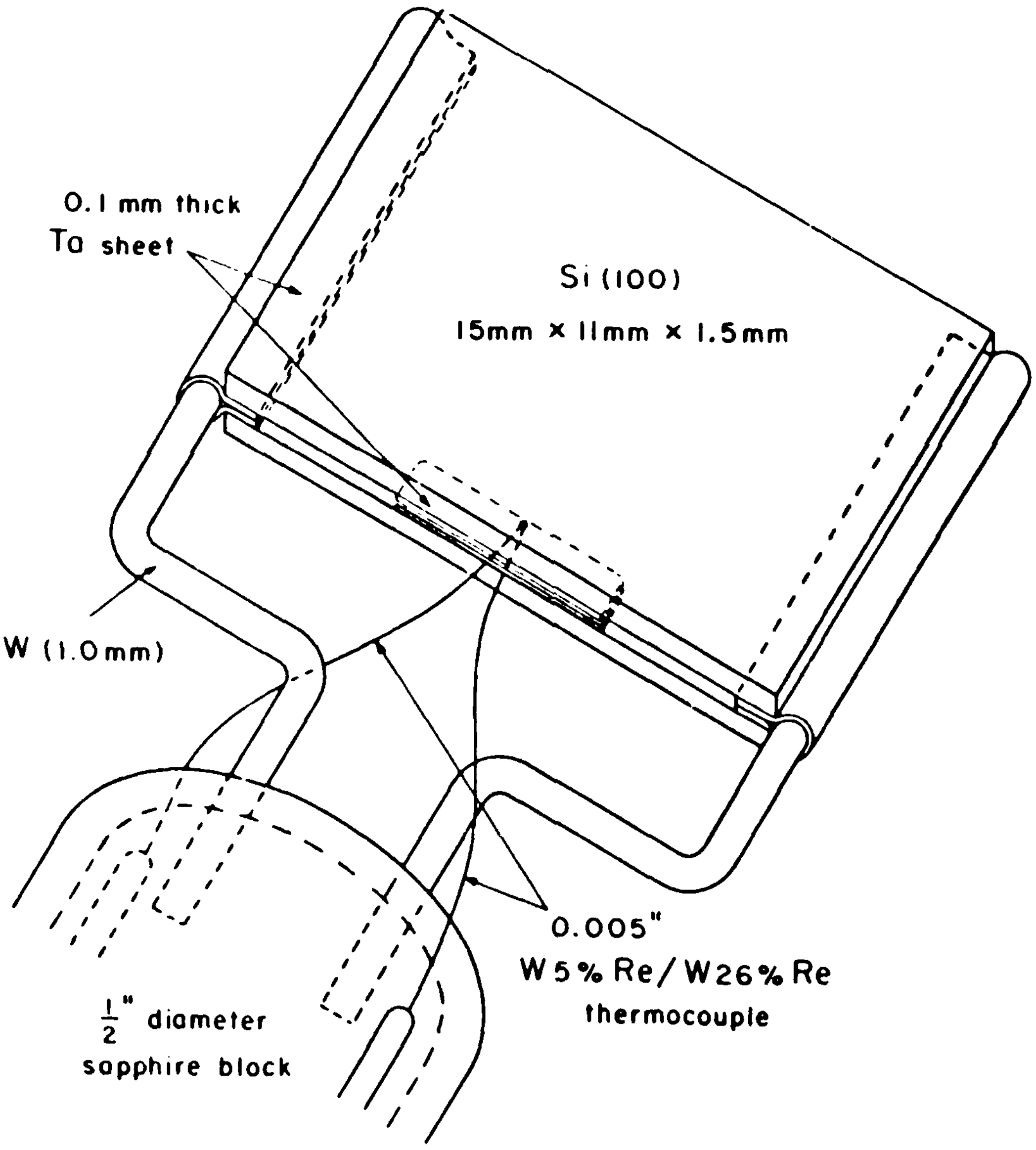

Figure 5.2

Thyristor Power Supply for the Resistive Heating of Semiconductor Samples

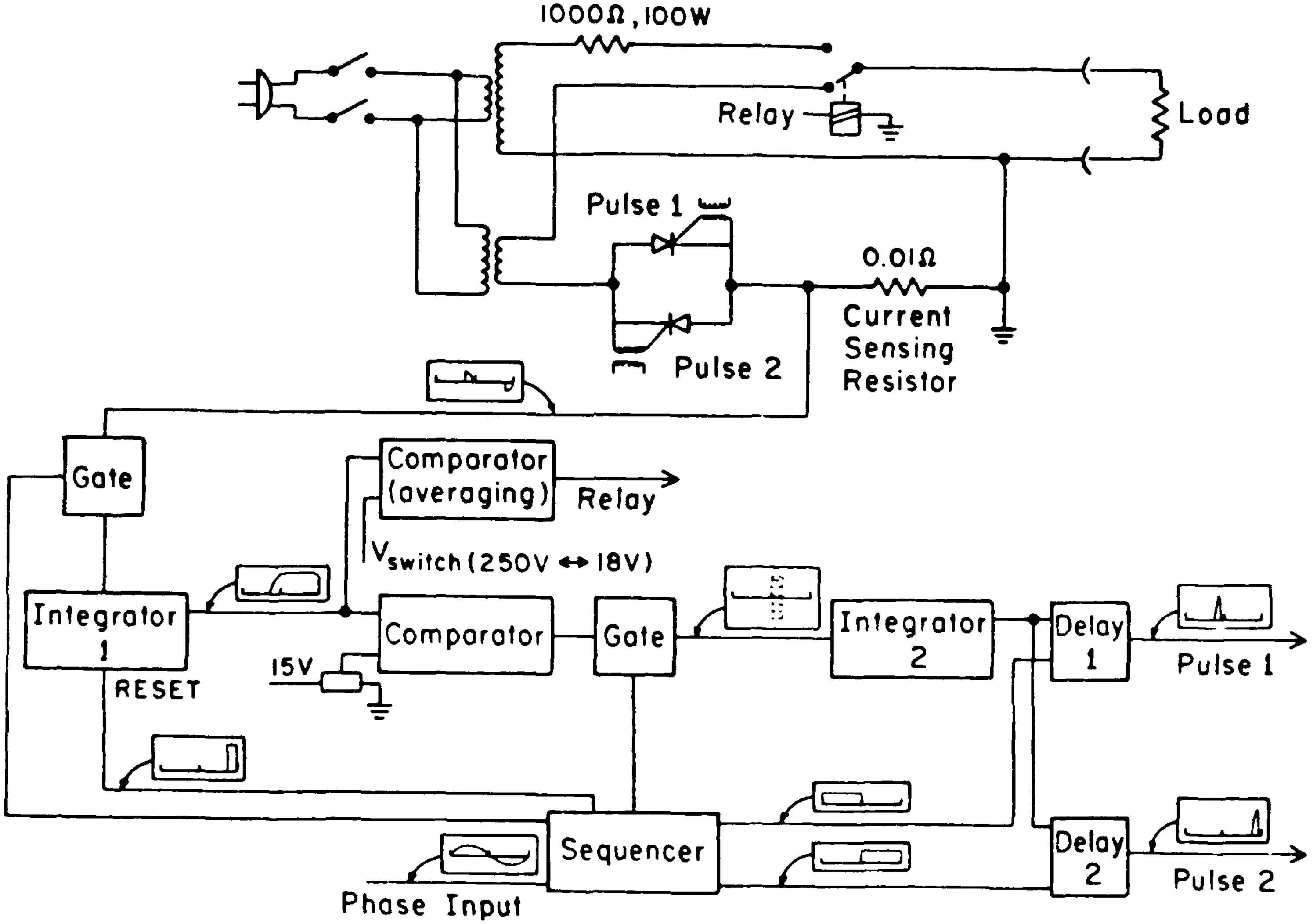

Figure 5.3

SCHEMATIC DIAGRAM OF
MOLECULAR BEAM DOSER – GAS HANDLING SYSTEM

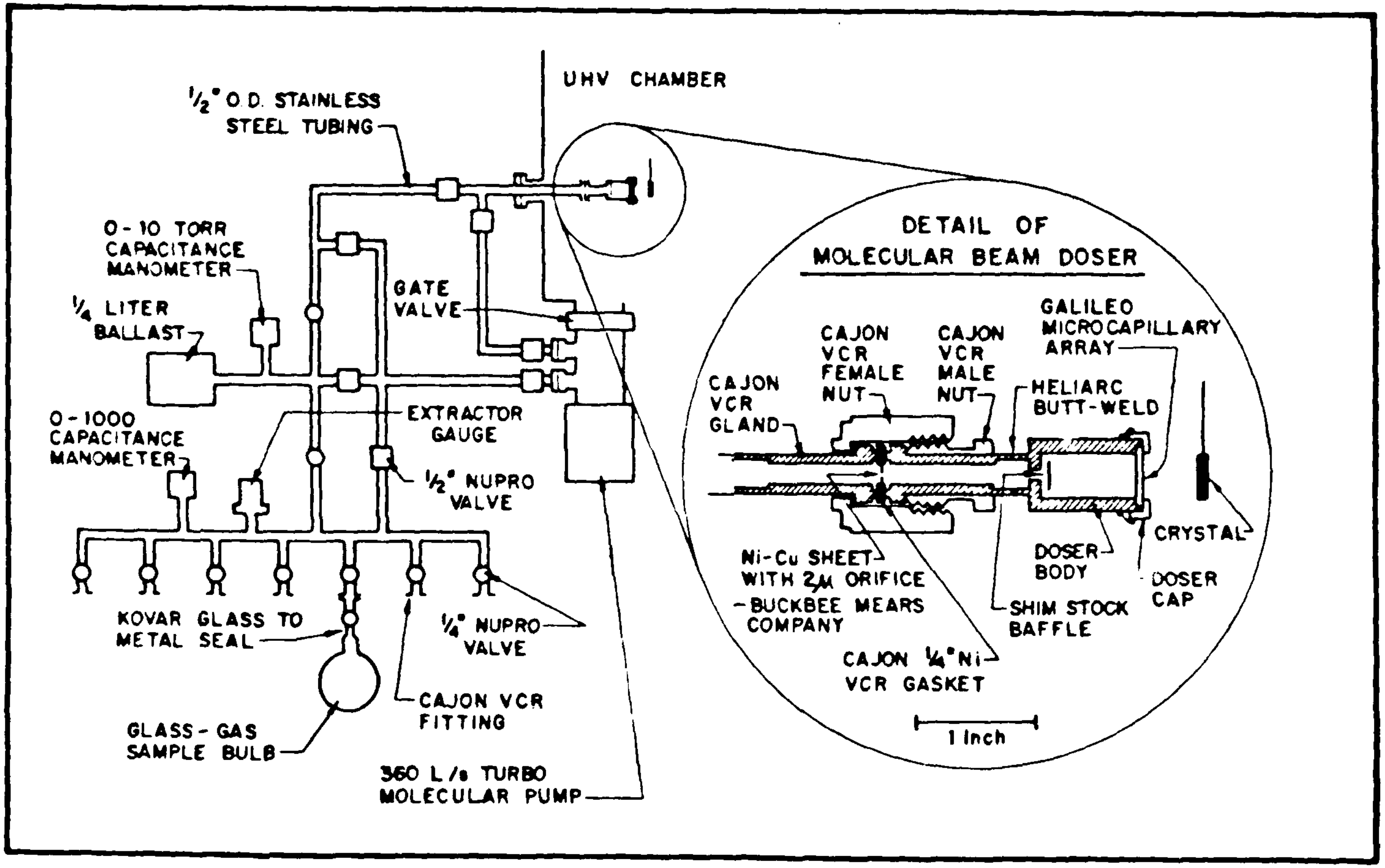

Figure 5.4

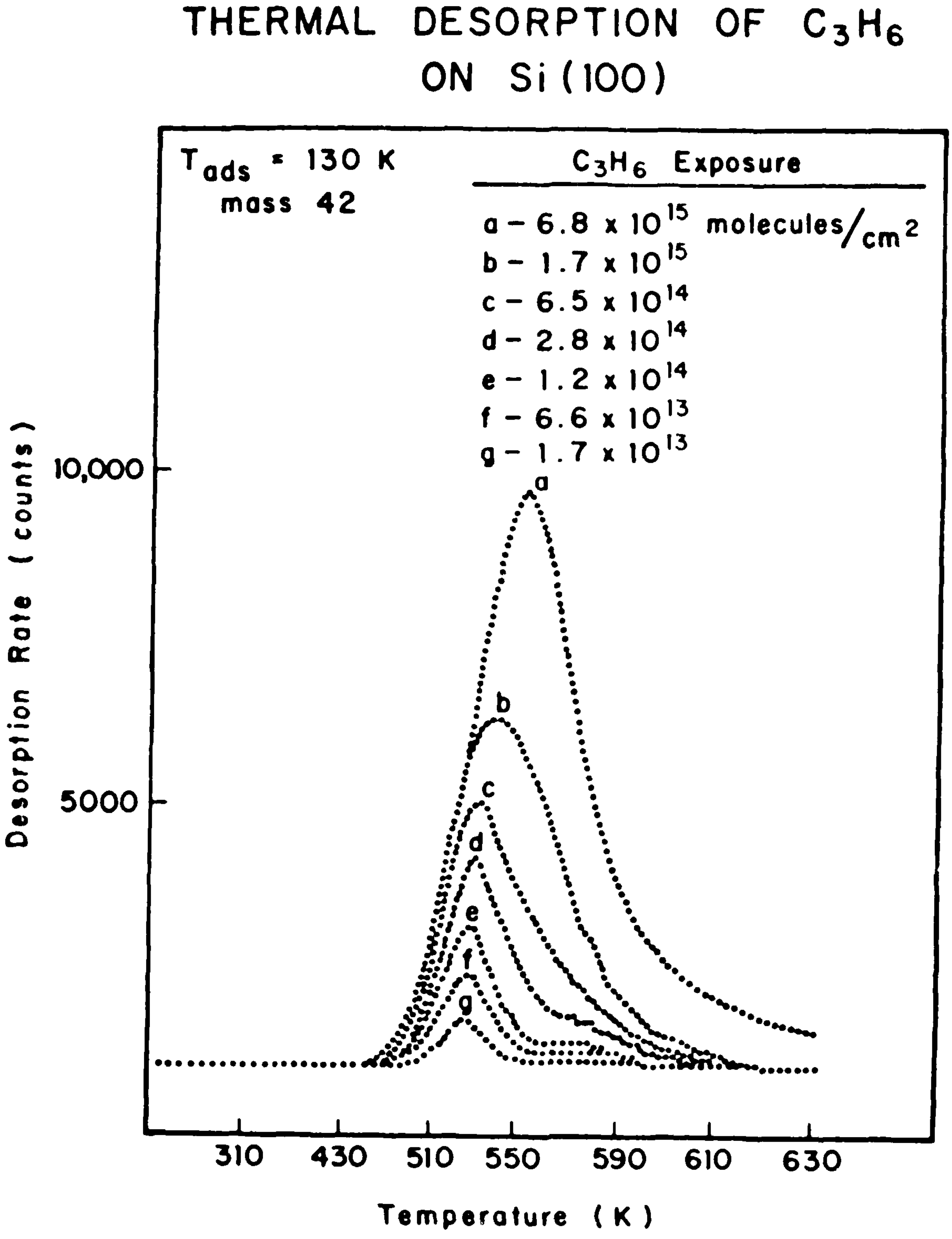
THERMAL DESORPTION OF C_3H_6 ON Si(100)
T_{ads} = 130 K
mass 42
C_3H_6 Exposure
a – 6.8 x 10^{15} molecules/cm^2
b – 1.7 x 10^{15}
c – 6.5 x 10^{14}
d – 2.8 x 10^{14}
e – 1.2 x 10^{14}
f – 6.6 x 10^{13}
g – 1.7 x 10^{13}
10,000
5000
Desorption Rate (counts)
a
b
c
d
e
f
g
310
430
510
550
590
610
630
Temperature (K)

Figure 5.5

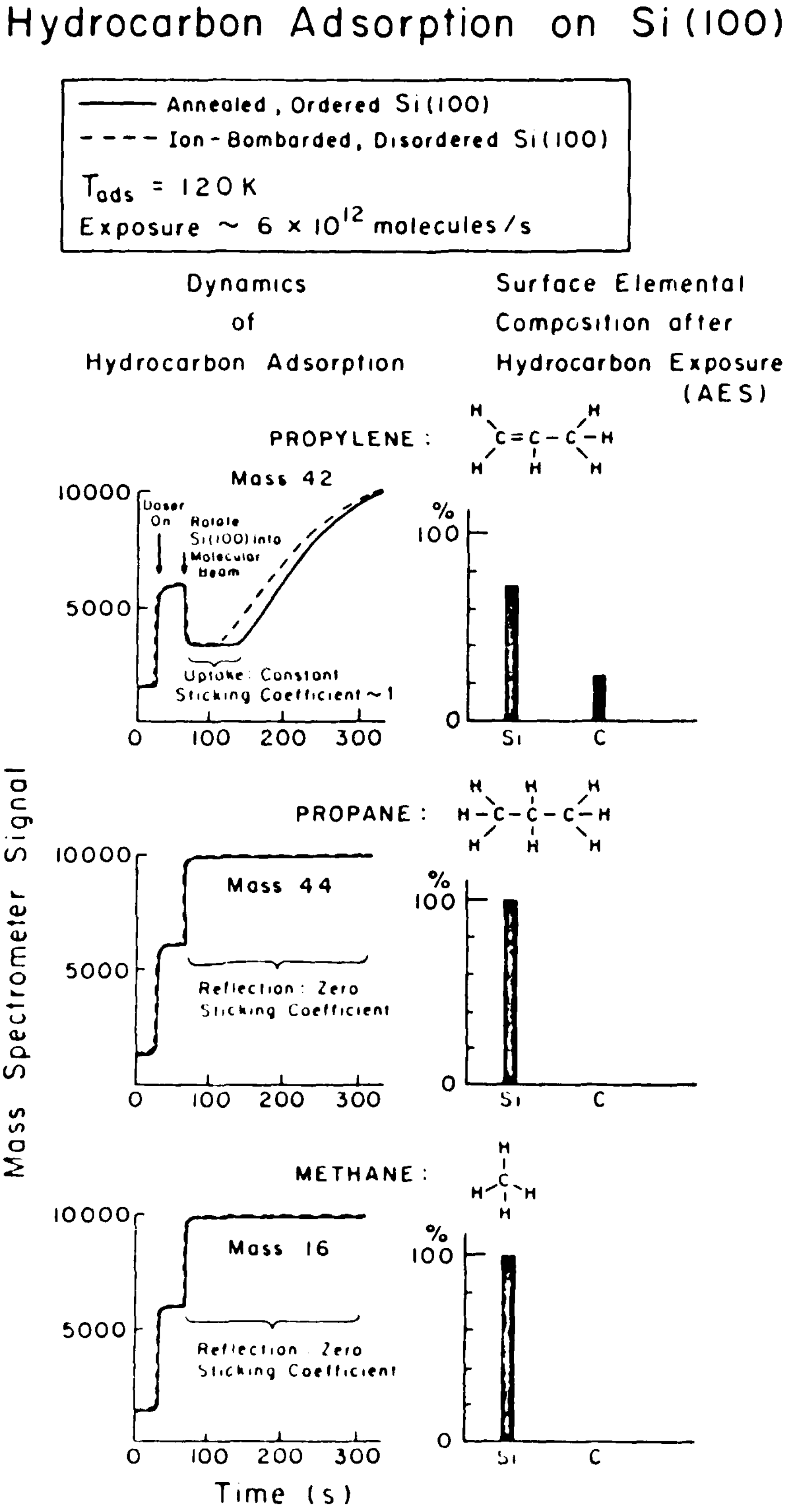
Hydrocarbon Adsorption on Si(100)
Annealed, Ordered Si(100)
Ion-Bombarded, Disordered Si(100)
T_{ads} = 120 K
Exposure ~ 6 × 10^{12} molecules/s
Dynamics of Hydrocarbon Adsorption
Surface Elemental Composition after Hydrocarbon Exposure (AES)
PROPYLENE:
Mass 42
Doser On
Rotate Si(100) into Molecular Beam
Uptake: Constant Sticking Coefficient ~ 1
10000
5000
0
100
200
300
%
100
0
Si
C
PROPANE:
Mass 44
Reflection: Zero Sticking Coefficient
METHANE:
Mass 16
Reflection: Zero Sticking Coefficient
Mass Spectrometer Signal
Time (s)

Figure 5.6

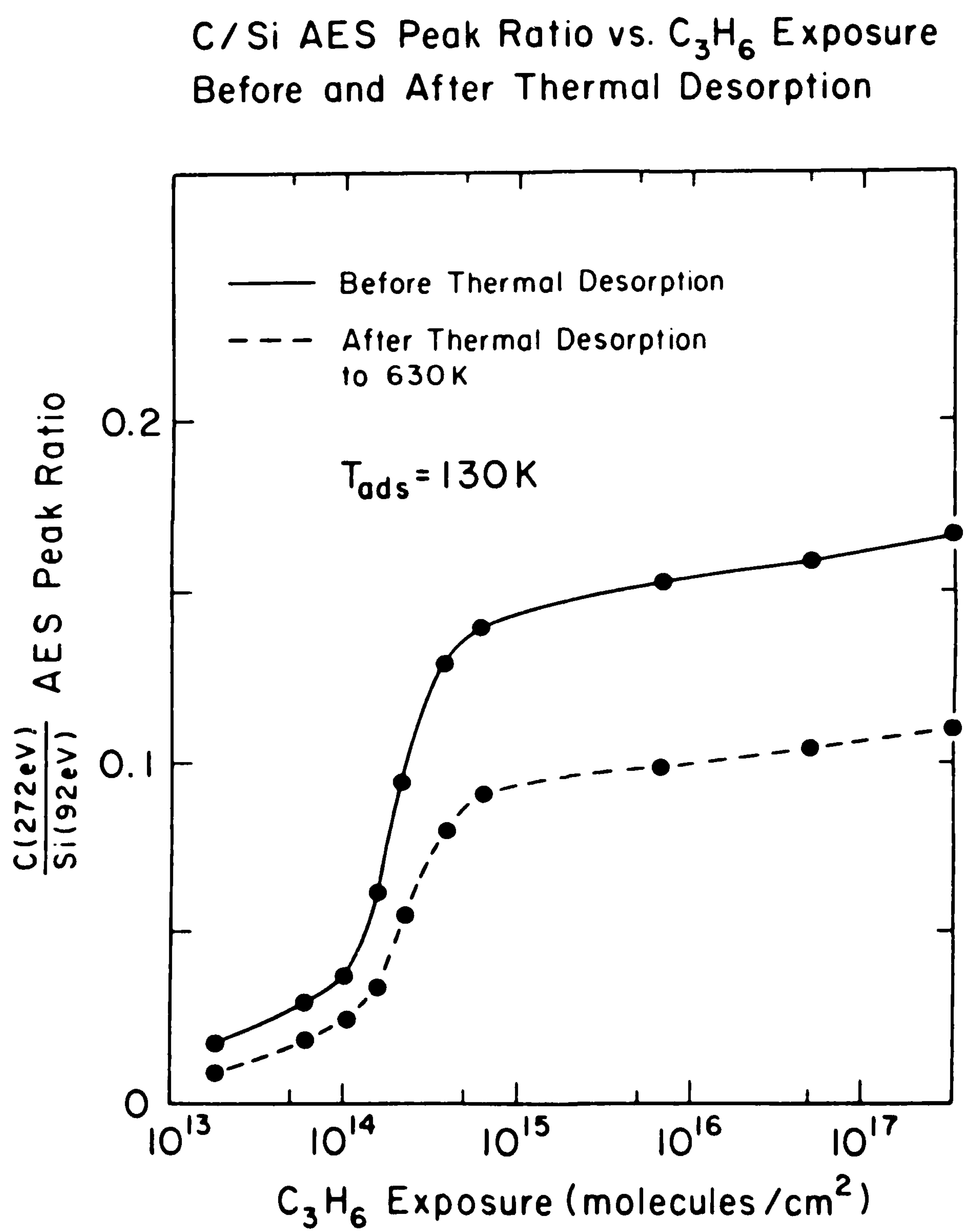
C/Si AES Peak Ratio vs. C_3H_6 Exposure
Before and After Thermal Desorption
Before Thermal Desorption
After Thermal Desorption to 630K
T_{ads} = 130K
$\frac{C(272eV)}{Si(92eV)}$ AES Peak Ratio
0
0.1
0.2
10^{13}
10^{14}
10^{15}
10^{16}
10^{17}
C_3H_6 Exposure (molecules/cm^2)

Figure 5.7

Effect of Surface Disordering on Thermal Desorption of C_3H_6 on Si(100)

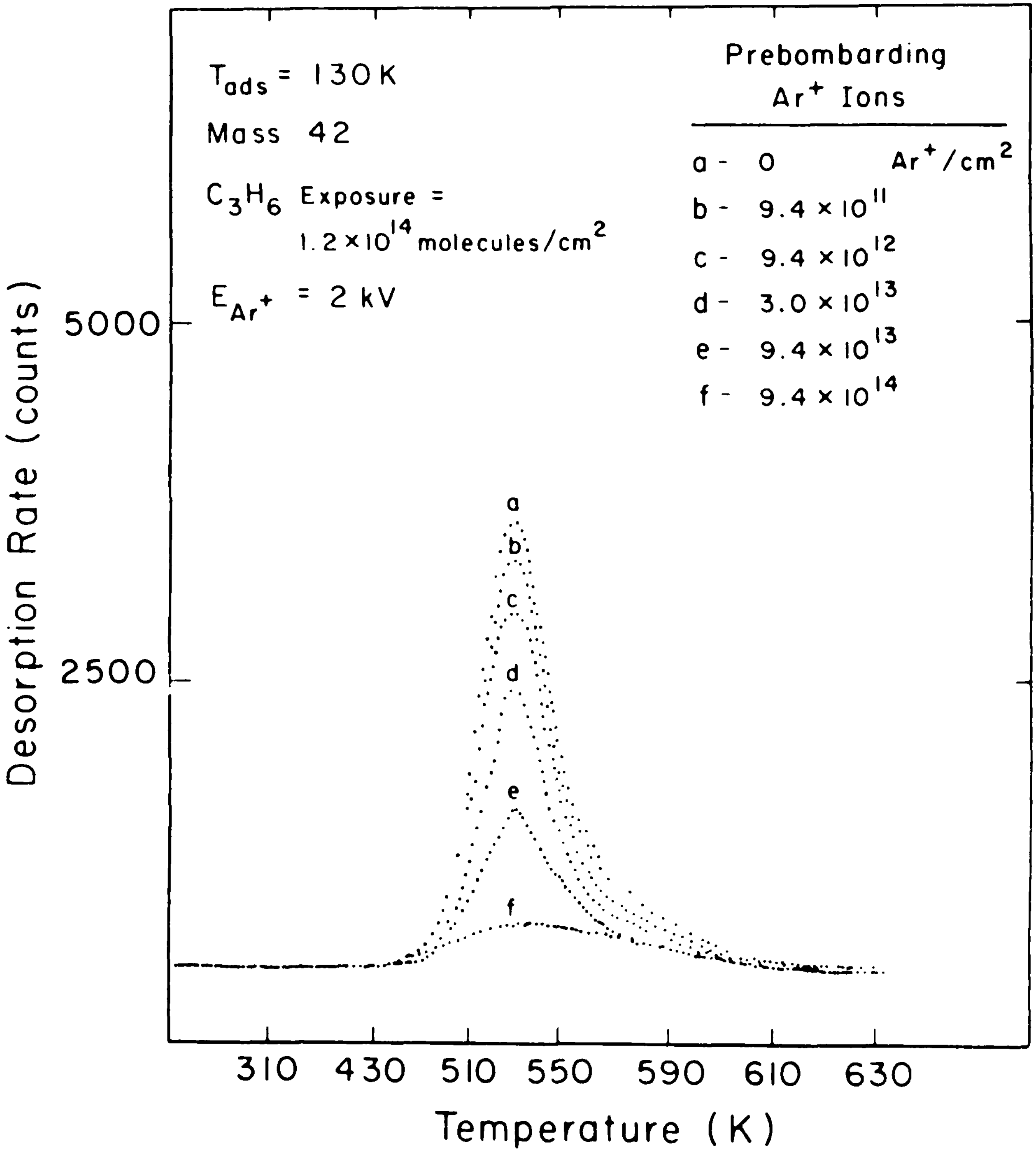

Figure 5.8

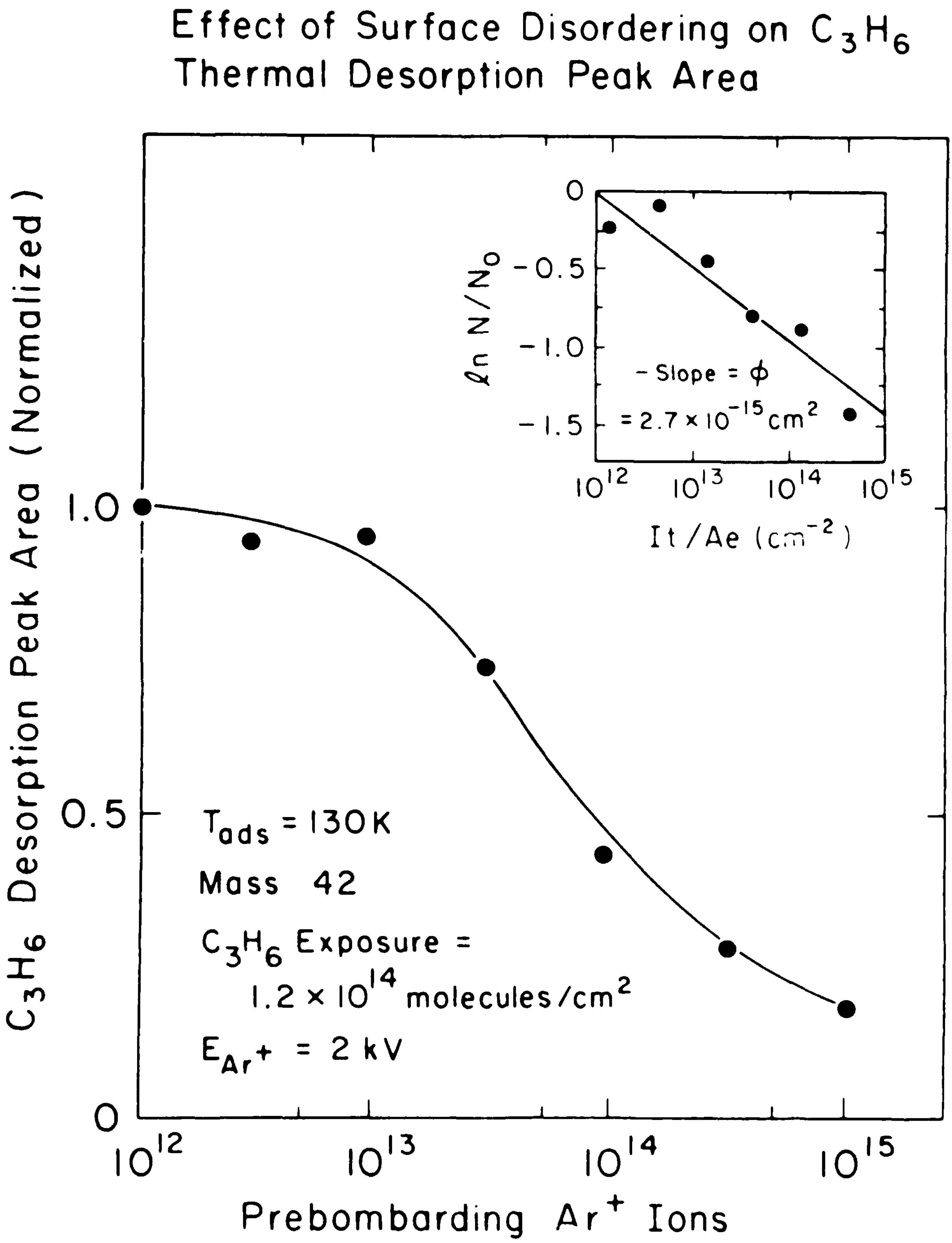
Effect of Surface Disordering on C_3H_6 Thermal Desorption Peak Area
C_3H_6 Desorption Peak Area (Normalized)
1.0
0.5
0
10^{12}
10^{13}
10^{14}
10^{15}
Prebombarding Ar^+ Ions
T_{ads} = 130K
Mass 42
C_3H_6 Exposure = 1.2×10^{14} molecules/cm^2
E_{Ar^+} = 2 kV
$\ell n\ N/N_0$
0
−0.5
−1.0
−1.5
− Slope = ϕ = $2.7 \times 10^{-15} cm^2$
10^{12}
10^{13}
10^{14}
10^{15}
It/Ae (cm^{-2})

Figure 5.9

Effect of Preadsorbed Atomic Hydrogen on Thermal Desorption of C_3H_6 on Si(100)

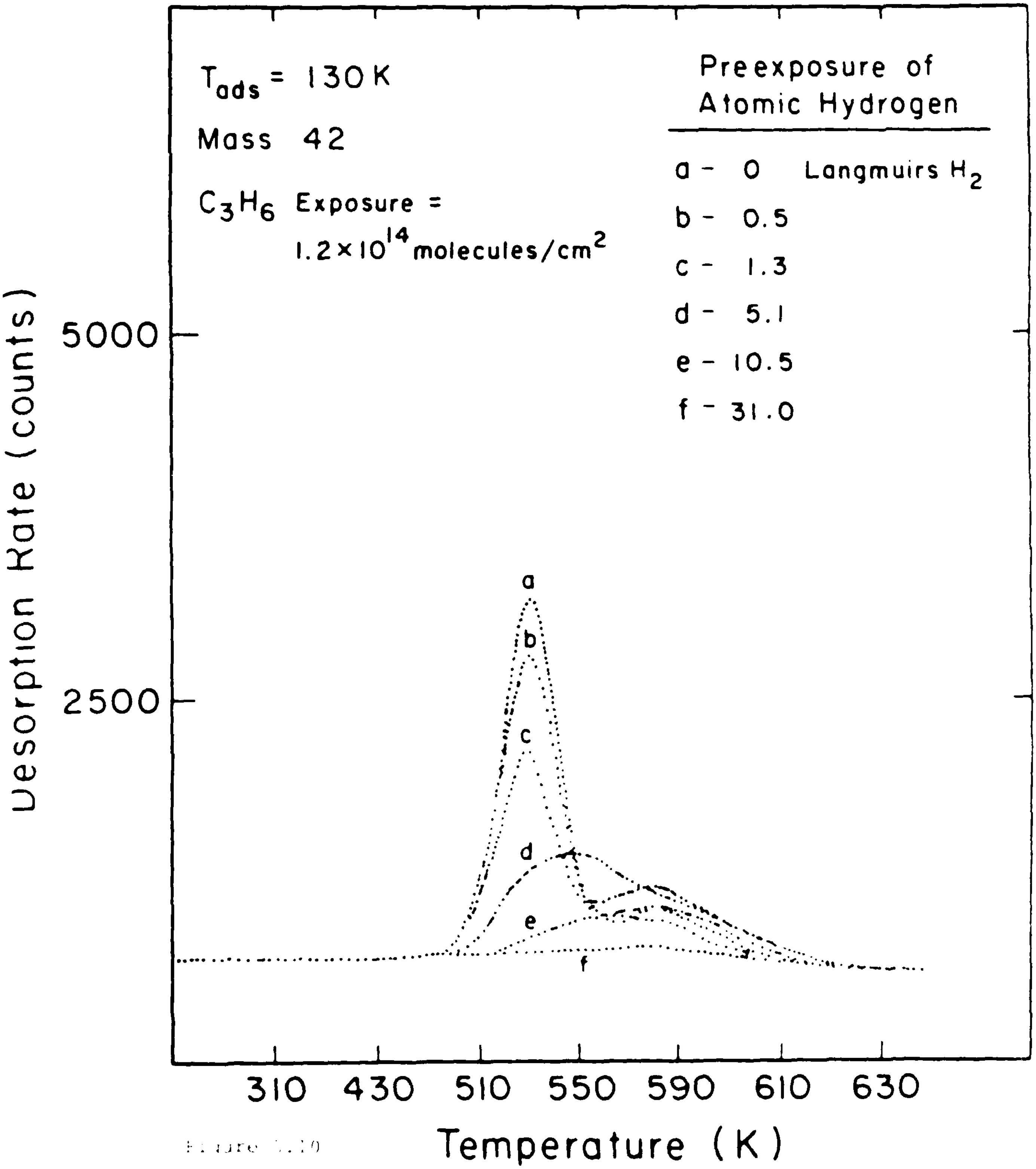

Figure [illegible].10

EFFECT OF ELECTRON IRRADIATION ON THERMAL DESORPTION OF C_3H_6 ON Si(100)

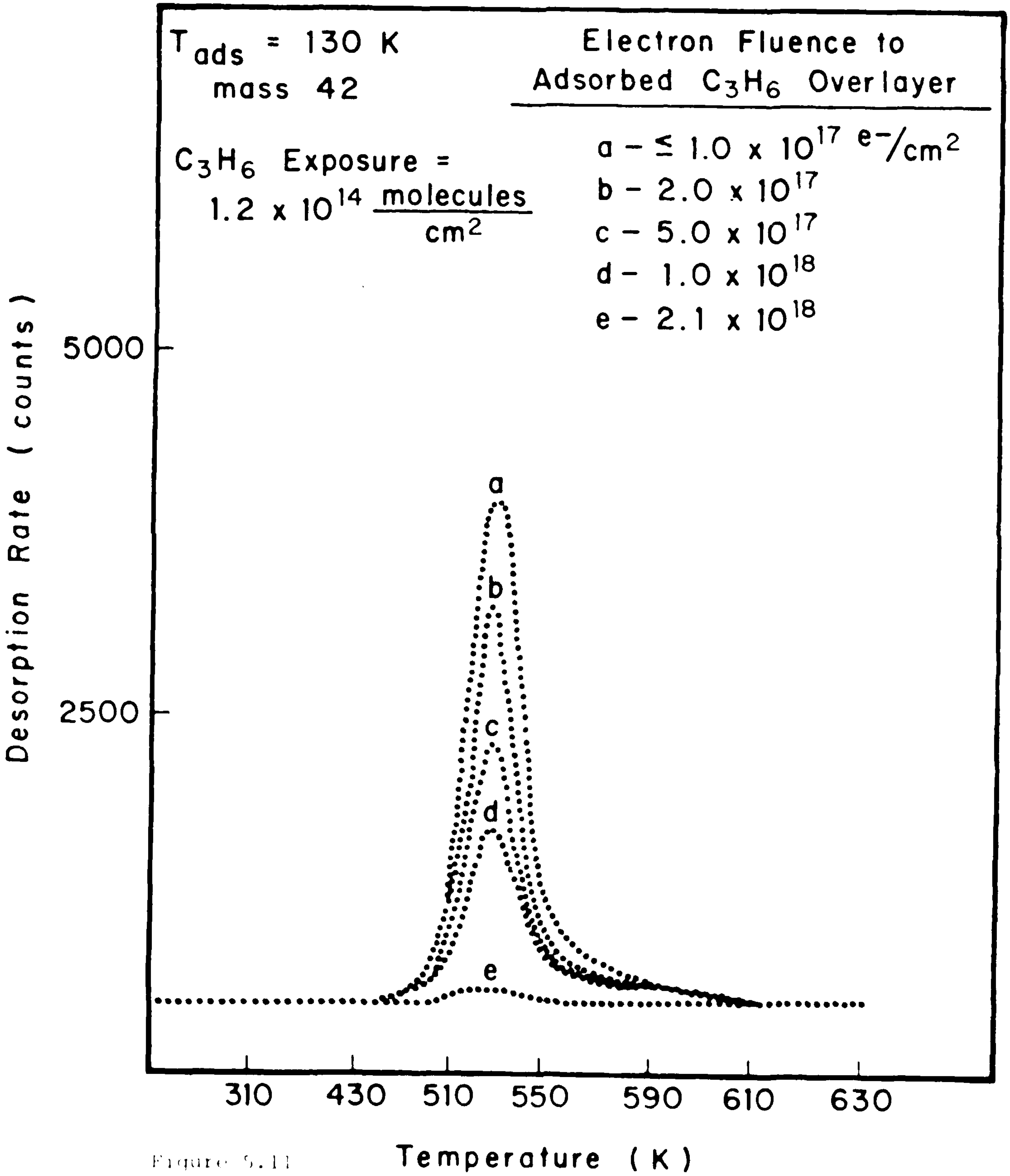

Figure 5.11

Effect of Electron Irradiation on C_3H_6 Thermal Desorption Peak Area

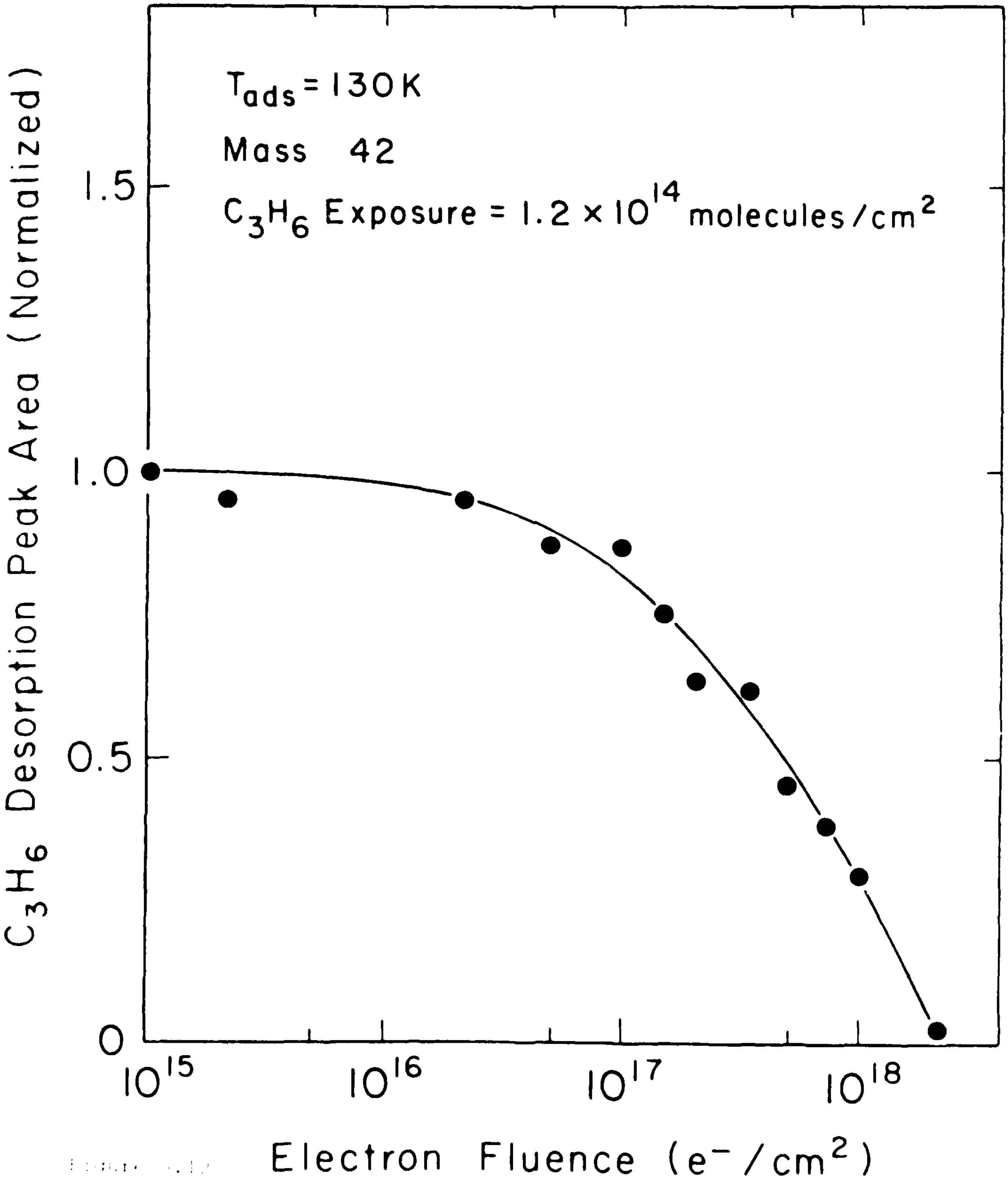

Figure [illegible]

END

FILMED

FEB. 1988

DTIC